

ASOD60K: An Audio-Induced Salient Object Detection Dataset for Panoramic Videos

Yi Zhang¹

© The Author(s) 2021. This article is published with open access at Springerlink.com

Abstract Exploring to what humans pay attention in dynamic panoramic scenes is useful for many fundamental applications, including augmented reality (AR) in retail, AR-powered recruitment, and visual language navigation. With this goal in mind, we propose **PV-SOD**, a new task that aims to segment salient objects from panoramic videos. In contrast to existing fixation-/object-level saliency detection tasks, we focus on audio-induced salient object detection (SOD), where the salient objects are labeled with the guidance of audio-induced eye movements. To support this task, we collect the first large-scale dataset, named *ASOD60K*, which contains 4K-resolution video frames annotated with a six-level hierarchy, thus distinguishing itself with richness, diversity and quality. Specifically, each sequence is marked with both its super-/sub-class, with objects of each sub-class being further annotated with human eye fixations, bounding boxes, object-/instance-level masks, and associated attributes (*e.g.*, geometrical distortion). These coarse-to-fine annotations enable detailed analysis for PV-SOD modeling, *e.g.*, determining the major challenges for existing SOD models, and predicting scanpaths to study the long-term eye fixation behaviors of humans. We systematically benchmark 11 representative approaches on *ASOD60K* and derive several interesting findings. We hope this study could serve as a good starting point for advancing SOD research towards panoramic videos. The dataset and benchmark will be made publicly available at <https://github.com/PanoAsh/ASOD60K>.

Keywords 360° video salient object detection, saliency detection, panoramic videos, benchmark.

¹ Institut National des Sciences Appliquées de Rennes (INSA Rennes), France.

Manuscript received: 2021-07-24; accepted: 2021-XX-XX.

1 Introduction

Recently, AI companies and manufacturers have developed several panoramic cameras, such as Facebook's Surround360, Insta360 One, Ricoh Theta, and Google Jump VR, which produce omnidirectional¹ images (Fig. 1 (b)) capturing a scene with a $360^\circ \times 180^\circ$ field-of-view (FoV). Thus, exploring human attention in dynamic scenes captured by these devices is of significant importance to augmented/virtual reality (AR/VR) applications, *e.g.*, shopping, online recruitment, piloting [32], automatic cinematography [67], and immersive games.

In practice, we have found that existing object-level saliency detection (*i.e.*, SOD) techniques and the datasets that underpin their progress are subject to two important limitations. First, the input source only includes the *visual information* from images (*e.g.*, I-SOD (Image SOD) [1, 2, 17, 76], CoSOD [20, 21, 25], RGB-D SOD [22, 27, 28, 50, 59, 101], RGB-T SOD [68, 71], LFSOD [38, 60], HRSOD [91, 93], Remote Sensing SOD [94]), or videos (*e.g.*, V-SOD (Video SOD) [23, 36, 74]) ignoring the *auditory cues* that are ubiquitous in dynamic scenes [69, 70, 72]. Furthermore, all the above mentioned SOD tasks focus on 2D images/videos, which are regarded as perspective images with local FoVs (compared with $360^\circ \times 180^\circ$ FoV), thus failing to capture the surrounding context and corresponding layout of immersive real-life daily scenes. However, these rich global geometrical cues are crucial for human attention modeling.

To this end, we envision that segmenting salient objects from panoramic videos with *audio-visual* data will benefit not only our research community but also commercial products. To facilitate the study of **panoramic video salient object detection (PV-SOD)**, we collect *ASOD60K*², the first large-scale

¹In the following sections, we use 'omnidirectional', 'panoramic', and '360°' interchangeably.

²Collecting the six types of labels was a costly and time-

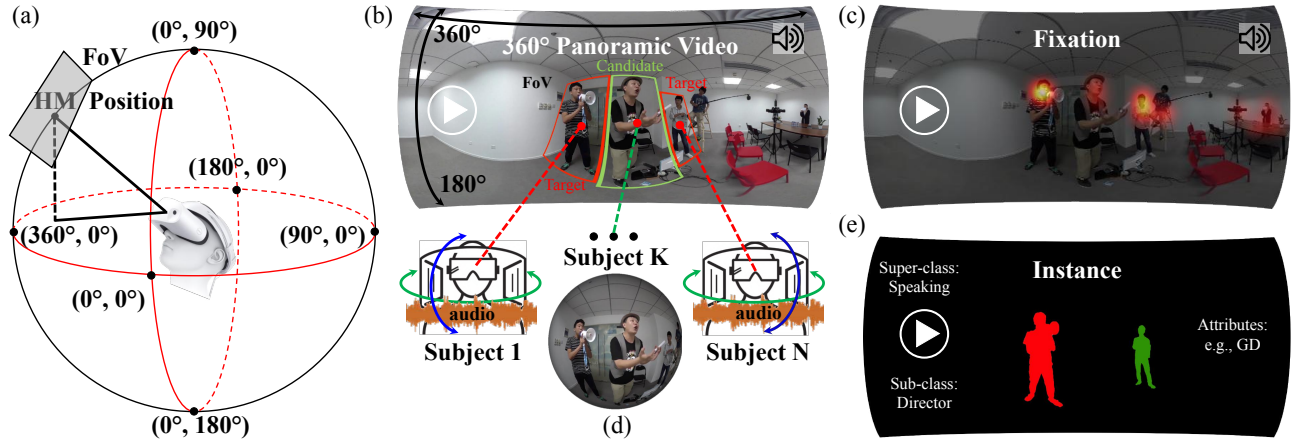


Fig. 1 Annotation examples from the proposed *ASOD60K* dataset. (a) Illustration of head movement (HM) [85]. The subjects wear Head-Mounted Displays (HMDs) and observe $360^\circ \times 180^\circ$ scenes by moving their head to control a field-of-view (FoV) in the range of $360^\circ \times 180^\circ$. (b) Each subject (*i.e.*, Subject 1 to Subject N) watches the video without restriction. (c) The HMD-embedded eye tracker records their eye fixations. (d) According to the fixations, we provide coarse-to-fine annotations for each FoV including (e) super/sub-classes, instance-level masks and attributes (*e.g.*, GD-Geometrical Distortion).

PV-SOD dataset providing professional annotations. *ASOD60K* has several distinctive features:

- **Hierarchical categories.** All videos in the database are labeled in a hierarchical manner, *i.e.*, with the *super-class* and *sub-class*. The two-level semantic categories provide a solid foundation for not only weakly supervised approaches but also fully supervised models.
- **Diverse annotations.** For each video sequence/frame, we provide coarse-to-fine annotations, including the subjects' head movement (HM) and eye fixations, bounding boxes, object-level masks, and instance-level labels, which can greatly benefit different vision tasks (*e.g.*, scanpath prediction, fixation prediction, SOD and salient instance detection).
- **Attribute labels.** Each sequence is annotated with specific attributes, *e.g.*, *geometrical distortion*, *occlusions*, and *motion blur*. Combined with the performance of the evaluated models, these attributes (Tab. 2 & Fig. 2) shed new light on the experimental analysis.
- **High quality.** All video sequences are in high-resolution (4K) to adapt to VR devices such as Head-Mounted Displays (HMDs). Moreover, cross-checking (*i.e.*, more than three-fold) by multiple experts and volunteers is conducted to maintain reliability, accuracy, and consistency during the whole annotation process.

The aforementioned aspects together provide important support for studying human attention consuming work, and it took us about 1 year to set up this large-scale database.

in panoramic videos. Further, we summarize the design rules that a balanced PV-SOD dataset should fulfill, which can be used as reference for similar fields when collecting and labeling data.

To reveal the challenges of PV-SOD, we perform a set of empirical studies based on the collected *ASOD60K* dataset. We obtain three interesting observations. i) According to the overall ($S_\alpha < 0.7$) and attribute-based performance of the tested models, this task is still far from being solved. ii) We find that the eye fixations with audio are relatively consistent across subjects while the data without audio exhibit large fluctuations between different subjects. iii) A sparsely labeled database is more beneficial for image-based models but more challenging for video-based models. These findings clearly show the challenges of salient object detection in panoramic videos.

In a nutshell, our main contributions are twofold: i) We introduce *ASOD60K*, the first *large-scale* dataset for PV-SOD, which consists of 62,455 high-resolution (4K) video frames from 67 carefully selected 360° panoramic video sequences. 10,465 key frames are annotated with rich labels, namely, *super-class*, *sub-class*, *attributes*, *HM data*, *eye fixations*, *bounding boxes*, *object masks*, and *instance masks*. ii) Based on the established *ASOD60K*, we present a comprehensive study on 11 representative models, which serves as the first standard leaderboard. Based on the evaluation results, we present insightful conclusions that may inspire novel ideas toward new research directions.

Tab. 1 Summary of widely used salient object detection (SOD) datasets and the proposed panoramic video SOD (PV-SOD) dataset. #Img: The number of images/frames. #GT: The number of ground-truth masks. Pub. = Publication. Obj.-Level = Object-Level. Ins.-Level = Instance-Level. Fix. GT = Fixation-guided ground truths. † denotes equirectangular (ER) images.

Dataset	Task	Year	Pub.	#Img	#GT	min(W, H)	max(W, H)	Obj.-Level	Ins.-Level	Attribute	Fix. GT	Audio
ECSSD [88]	I-SOD	2013	CVPR	1,000	1,000	139	400	✓				
DUT-OMRON [89]	I-SOD	2013	CVPR	5,168	5,168	139	401	✓			✓	
SegTrack V2 [41]	V-SOD	2013	ICCV	1,065	1,065	212	640	✓				
PASCAL-S [48]	I-SOD	2014	CVPR	850	850	139	500	✓			✓	
FBMS [54]	V-SOD	2014	TPAMI	13,860	720	253	960	✓				
HKU-IS [44]	I-SOD	2015	CVPR	4,447	4,447	100	500	✓				
MCL [40]	V-SOD	2015	TIP	3,689	463	270	480	✓				
ViSal [79]	V-SOD	2015	TIP	963	193	240	512	✓				
DAVIS2016 [58]	V-SOD	2016	CVPR	3,455	3,455	900	1,920	✓		✓		
DUTS [75]	I-SOD	2017	CVPR	15,572	15,572	100	500	✓				
ILSO [42]	I-SOD	2017	CVPR	1,000	1,000	142	400	✓	✓			
UVSD [51]	V-SOD	2017	TCSVT	3262	3262	240	877	✓				
SOC [17]	I-SOD	2018	ECCV	6,000	6,000	161	849	✓	✓	✓		
VOS [47]	V-SOD	2018	TIP	116,103	7,467	312	800	✓			✓	
DAVSOD [23]	V-SOD	2019	CVPR	23,938	23,938	360	640	✓	✓	✓	✓	
F-360I-SOD [95]	PI-SOD	2020	ICIP	107 [†]	107	1,024	2,048	✓	✓		✓	
360-SOD [46]	PI-SOD	2020	JSTSP	500 [†]	500	512	1,024	✓				
360-SSOD [53]	PI-SOD	2020	TVCG	1,105 [†]	1,105	546	1,024	✓				
ASOD60K (OUR)	PV-SOD	2021	CVMJ	62,455 [†]	10,465	1,920	3,840	✓	✓	✓	✓	✓

2 Related Work

Human attention modeling in panoramic videos can be roughly split into four levels: HM prediction [85], eye fixation/gaze prediction [81, 86], salient object detection (SOD), and salient instance detection. Our work mainly focuses on the object-level task, leaving other tasks to our future studies. In this section, we only briefly discuss some closely related works, *i.e.*, datasets, models, and techniques for 360° image processing.

2.1 Datasets

Image Salient Object Detection (I-SOD). The image-based SOD task has gained significant attention in the past few years. The remarkable progress of I-SOD is highly related to the development of several representative datasets [17, 42, 44, 48, 75, 88, 89]. ECSSD [88], DUT-OMRON [89], PASCAL-S [48], and HKU-IS [44] are four early, small-scale datasets with limited image resolution. To increase the amount of training data, DUTS [75] was introduced and has become one of the most popular benchmarks. Furthermore, ILSO [42] and SOC [17] were recently proposed with the goal of enabling not only object-level but also instance-level SOD tasks. We refer the reader to the survey paper by [76] for a thorough review.

Video Salient Object Detection (V-SOD). In addition to I-SOD datasets, several V-SOD benchmarks have also been introduced. Tab. 1 summarizes their details. As can be seen, DAVSOD [23] is the largest dataset and provides comprehensive annotations for the V-SOD task.

Panoramic Image Salient Object Detection (PI-SOD). There are three attempts toward establishing datasets for 360° panoramic image-based SOD [46, 53, 95], all of which provide pixel-wise object-level ground truths (GTs) with similar resolution (*e.g.*, $\max(w, h) = 2,048$). 360-SOD [46] is the pioneering work for SOD in 360° scenes. It consists of 500 equirectangular (ER) images (the most widely used planar representation of 360° image without any loss of spatial information) representing both the indoor/outdoor scenes with object-level annotations. 360-SSOD [53] is a larger public PI-SOD dataset that has 1,105 semantically balanced panoramic (ER) images. Besides, F-360iSOD [95] is so far the only 360° image SOD dataset that provides pixel-wise instance-level GTs.

Other Datasets. Other closely related datasets are either designed to simulate human HM (360VHMD [11] and PVS-HMEM [85]), or eye fixations (*i.e.*, saliency detection) in 360°/panoramic images (Salient!360 [63]) or 360° videos (*e.g.*, Wild-360 [5], VR-Scene [86], 360-Saliency [96]). As far as we know, Chao *et al.*'s [3] work is the only 360° audio-visual saliency dataset, which contains 12 videos with HM-based annotations under mute, mono, and ambisonics modalities. Finally, datasets such as [7, 33, 90] focus on bounding-box-level object detection in 360°.

As summarized in Tab. 1, no work exists to study the segmentation of salient objects in free-viewing panoramic videos with audio. The closest works are audiovisual saliency detection from 2D videos [35, 70] in a plane and salient object detection in omnidirectional images [46, 53, 95] *without audio*. We refer readers to the survey paper about 360° data processing [16, 84] for



Fig. 2 Examples of challenging attributes (see Tab. 2) on ER images from our *ASOD60K*, with instance-level GT and fixations as annotation guidance. $f_{k,l,m}$ denote random frames of a given video. Best viewed in color. More examples are shown in Fig. 17.

more details.

2.2 SOD Models

Since no SOD approaches currently exist for the PV-SOD task, we present the SOD methodologies for I-SOD, V-SOD, and PI-SOD.

Algorithms for I-SOD. In the past few years, convolutional neural networks (CNNs) have been the most commonly used architecture in state-of-the-art (SOTA) I-SOD models [26, 29, 39, 49, 55, 61, 62, 77, 82, 83, 97, 100, 102, 103], which are trained on large-scale datasets (*e.g.*, DUTS [75]) in a fully supervised manner. ASNet [77] uses eye fixations to aid salient object localization, while models such as AFNet [26], BASNet [61], PoolNet [49], EGNNet [97], SCRNet [83], and LDF [80] emphasize object appearance (boundaries or skeletons) as guidance for the accurate segmentation of salient objects. With comparable accuracy, methods such as CPD [82], ITSD [100], and CSNet [29] also achieve improved inference speed.

Models for V-SOD. The recent development of large-scale video datasets such as DAVIS [58] and DAVISOD [23] have enabled deep learning-based V-SOD. Several works [43, 45, 87] have achieved success by introducing optical flow cues into the network. There is, however, the long-standing and often ignored issue of *saliency shift*, which was first highlighted and modeled in SSAV [23]. According to the open benchmark results,

COSNet [52], RCRNet [87], and PCSA [30] obtain best performances in the V-SOD task.

Methods for PI-SOD. To the best of our knowledge, DDS [46], stage-wise SOD [53] and FANet [34] are so far the only models exclusively designed for PI-SOD. They all emphasize the importance of mitigating the geometrical distortion brought by ER projection via specific modules.

2.3 360° Image Processing Approaches

The vast majority of current 360° image processing techniques are CNN-based, proposed for either ER or stereoscopic images (*e.g.*, spheres and icosahedrons).

CNNs on ER Images. ER projection is the most widely used approach for the 2D representation of a 360° image. It applies a uniform grid-based sampling method on the spherical surface, followed by an inevitable over-sampling of spherical regions near poles. Therefore, salient objects in ER images may suffer geometrical distortions to varying extents, depending on the distance between their geometrical locations and the equator of the ER image (Fig. 2). SphereNet [10], which consists of a location-adaptive kernel, was proposed for the classification and detection of objects in ER images. Similar location-dependent convolutional kernels are also applied in [65, 66].

CNNs on Stereoscopic Images. As there is no perfect 2D representation for 360° images, SO(3)-

based spherical CNNs [8, 15] were proposed to directly generalize convolutions on a sphere. However, these reparameterized 3D convolutional kernels hinder the use of classical backbones (*e.g.*, ResNet [31] or VGGNet [64]) pre-trained on large-scale datasets (*e.g.*, ImageNet [13]), which play an essential role in CNN-based SOD models (see Sec. 2.2). Recent researches [9, 37, 92] generalize convolutions on subdivided icosahedral faces, which contain much less geometrical distortion compared to ER images [14]. In addition, tangent image [14] was proposed to enable the implementation of semantic segmentation in 4K-resolution 360° images.

3 Proposed ASOD60K Dataset

We elaborate our *ASOD60K* in terms of stimuli collection, subjective experimentation, annotation pipeline and dataset statistics. Our goal is to introduce a new challenging dataset to the PV-SOD community.

3.1 Stimuli Collection

The stimuli of *ASOD60K* were searched on *YouTube* with different keywords (*e.g.*, 360°/panoramic/omnidirectional video, spatial audio, ambisonics [56]). As a result, our collected stimuli cover various real-world scenes (*e.g.*, indoor/outdoor scenes), different occasions (*e.g.*, sports, travel, concerts, interviews, dramas), different motion patterns (*e.g.*, static/moving camera), and diverse object categories (*e.g.*, humans, instruments, animals). They possess a wide range of major challenges found in 360° content³, providing us with a solid foundation to build a representative benchmark. In this way, we obtained about 1,000 noisy videos, *e.g.*, videos with a shaking camera, dark-screen transitions, without key content, displaying too many objects, of low quality. In line with the video dataset creation rules in [23, 78], we then carefully collected 67 high-quality video sequences with a total of 62,455 frames recorded with 62,455×40 HM and eye fixations. The 67 sequences are selected based on the following two criteria, 1) The source video must be in good visual quality, *i.e.*, 4K resolution for each video frame. 2) The scenes must include meaningful objects on which high saliency constantly focuses. In other words, scenes such as busy streets and carnivals where subjects' attention simultaneously scattering on multiple non-relevant objects, are removed from the dataset. Similar to [11], the frame rate of each collected video is not fixed

³Objects scattered far from the equator thus suffering from serious geometrical distortions in ER projections.

(varying from 24fps to 60fps), which did not influence the results of following subjective experiments since human attention is mainly event-related, rather than frame rate-dependent. Note that we manually trimmed the videos into small clips (29.6s on average) to avoid fatigue during the collection of human eye fixations. As a result, the final duration is 1983s in total.

3.2 Subjective Experimentation

Equipment. All the video clips were displayed using a HTC Vive HMD embedded with a Tobii eye tracker with 120Hz sample rate to collect eye fixations.

Observers. We recruited 40 participants (8 females and 32 males) aging from 18 to 34 years old who reported normal or corrected-to-normal visual and audio acuity. Twenty participants were randomly selected to watch videos with mono sound, while the other participants watched videos without sound. Note that the two groups own the same gender and age distributions. Hence, each video with each audio modality (*i.e.*, with or without sound) was viewed by 20 participants, and each participant viewed each video only once. We performed task-free viewing sessions.

Settings. All the participants seated in a swivel chair, wearing a HMD with headphones, and asked to explore the panoramic videos without any specific intention. During the experiments, the starting position was fixed to the center ($\theta = 0^\circ$ and $\phi = 0^\circ$) at the beginning of every video display. To avoid motion sickness and eye fatigue, we inserted a short rest of a five-second gray screen between two successive videos and a long break of 20 minutes after every 20 videos. We calibrated the system for each participant at the beginning and end stage of every long break.

3.3 Professional Annotation

Super-/Sub-Class Labeling. As shown in Fig. 3, our *ASOD60K* contains 67 videos representing three super-categories of audio-introduced scenes, including speaking (*e.g.*, monologue, conversation), music (*e.g.*, human singing, instrument playing) and miscellanea (*e.g.*, the sound of vehicle engines and horns on the streets, crowd noise in the open air). Each video is named in terms of its audio-visual information.

Head Movement and Eye Fixations. The recent video object segmentation dataset DAVIS [58] contains only one or several foreground objects per frame, where the salient objects can be easily defined. In contrast, other recent video SOD datasets, such as VOS [47] and DAVSOD [23], collect video stimuli representing more challenging scenes with multiple salient objects. In such

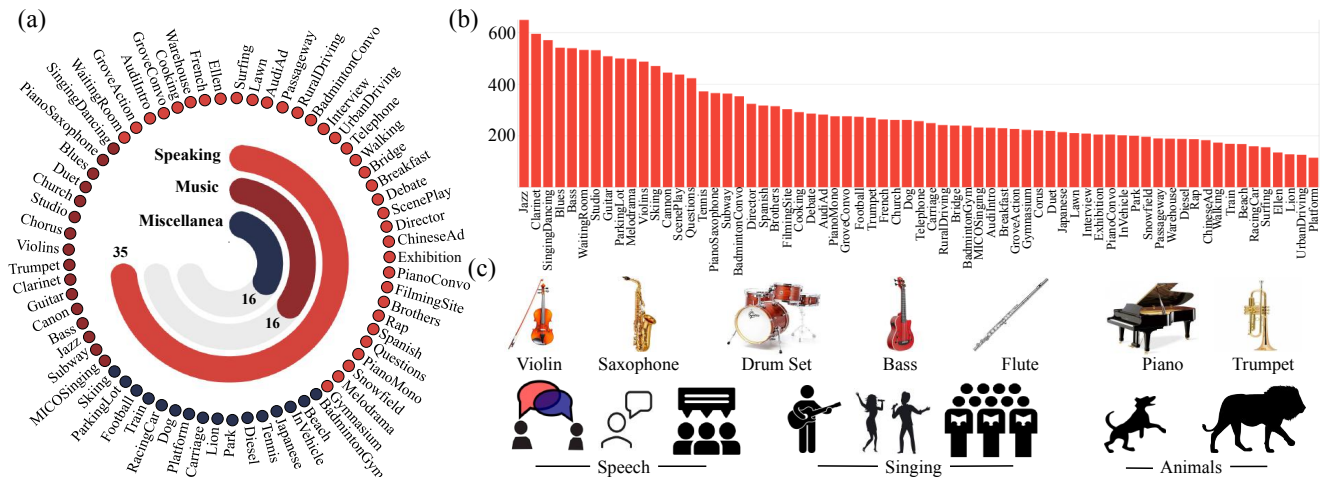


Fig. 3 Statistics of the proposed *ASOD60K*. (a) Super-/sub-category information. (b) Instance density of each sub-class. (c) Main sound sources of *ASOD60K* scenes, such as musical instruments, human instances and animals. Best viewed in color.

cases, fixation-based annotations (*e.g.*, saliency-shift [23]) are used as guidance to alleviate the ambiguity of defining salient objects. Based on the subjects' per-frame HM and eye fixations gained by conducting the subjective experiments (Sec. 3.2) with audio-visual stimuli, we produced the final annotations. Specifically, inspired by the experimental IoU threshold, *i.e.*, AP50 (threshold set as 50%), which is widely used in the field of object detection, we choose to keep the 50% of the smoothed fixation map regions which thus covers the top 50% of the saliency. In this way, we regard the top 50% saliency as high saliency and locate the salient objects overlapped with the high saliency regions.

Bounding Box Annotations. Generally, there are two types of labels in 360° object detection, *i.e.*, bounding FoVs [7, 90, 98] and bounding boxes [90]. As the vast majority of our collected video frames contain multiple salient objects near the 360 camera, bounding FoVs may introduce serious annotation ambiguities due to the divergence of projection angle selections between multiple annotators [90], thus not being suitable for the salient object annotation in the scenes from our *ASOD60K*. Following [90], we directly annotated the salient objects with bounding boxes in *ER* images.

Tab. 2 Attributes description (see examples in Fig. 2).

Att.	Description
MO	<i>Multiple Objects.</i> \geq three objects occur simultaneously.
OC	<i>Occlusions.</i> Object is partially occluded.
LS	<i>Low Space.</i> Object occupies $\leq 0.5\%$ of image area.
MB	<i>Motion Blur.</i> Moving object with fuzzy boundaries.
OV	<i>Out-of-View.</i> Object is cut in half in <i>ER</i> projection.
GD	<i>Geometrical Distortion.</i> Distorted object in <i>ER</i> projection.
CS	<i>Competing Sounds.</i> Sound objects compete for attention.

Our annotation protocol is threefold: i) We uniformly extracted 10,465 key frames from the total 62,455 frames with a sampling rate of 1/6. ii) We filtered the Gaussian-smoothed eye fixation maps corresponding to each of the key frames. iii) We adopted the widely used CVAT toolbox as our annotation platform, and recruited an expert to manually annotate the bounding box of each salient object in each of the *ER* key frames, under the guidance of the corresponding fixations overlaid (see Fig. 2). Finally, we obtained total 19,904 salient objects labeled with instance-level bounding boxes from 10,465 key frames. To the best of our knowledge, this is the first attempt to annotate salient objects with the guidance of audio-visual attention data.

Object-Level Annotations. With the coarse annotations (*i.e.*, bounding boxes) in hand, we needed to further label the data in a fine manner. Thus, three experts were recruited to manually annotate the salient objects in the $\sim 10K$ key frames. To ensure satisfying annotations, they were first required to pass a training session⁴ during which they had to correctly segment (by finely tracing objects' boundaries rather than drawing rough polygons) all the salient objects in a given video (previously shown to three senior researchers, with GTs acquired by consistent opinions), with the guidance of overlaid per-frame bounding boxes. Followed by a session during which they were asked to annotate all the defined salient objects in the rest of the panoramic videos. Finally, a thorough inspection was conducted by the same three senior researchers, to ensure the accuracy of the annotations. Following the same

⁴Note that it took the experts about 10 hours.

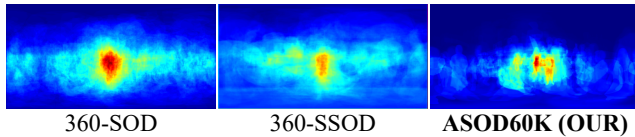


Fig. 4 Average object-level GT maps of 360-SOD [46], 360-SSOD [53] and our *ASOD60K*.

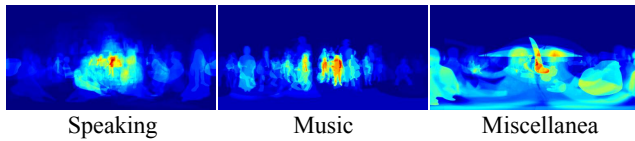


Fig. 5 The average object-level GT maps of our *ASOD60K* at super-class level.

pipeline as [20], we obtained 10,465 object annotations.

Instance-Level Annotations. Another three well-trained experts were then recruited to further draw pixel-wise instance-level masks by carefully tracing boundaries (rather than rough polygons) of the defined salient objects in each of the 10,465 key frames. To ensure high quality annotations, all the masks were sent to a quality check procedure implemented by the same three senior researches. As a result, we acquired 19,904 instance-level masks representing all the salient objects in all the 10,465 key frames (the number of instances in each video are shown in Fig. 3 (b)). Further, to refine the annotations quality, we transferred all the instance-level masks to object-level binary masks. The bounding boxes were also refined by the object-level masks. Please refer to Fig. 17 for annotation examples.

Attribute Labels. Following two large-scale video object segmentation datasets [23, 58], we also provide seven attributes in the proposed *ASOD60K*, including *multiple objects (MO)*, *occlusions (OC)*, *low space (LS)*, *out-of-view (OV)*, *motion blur (MB)*, *geometrical distortion (GD)* and *competing sounds (CS)* (Table 2). It is worth mentioning that, *OV* and *GD* (Fig. 2) are

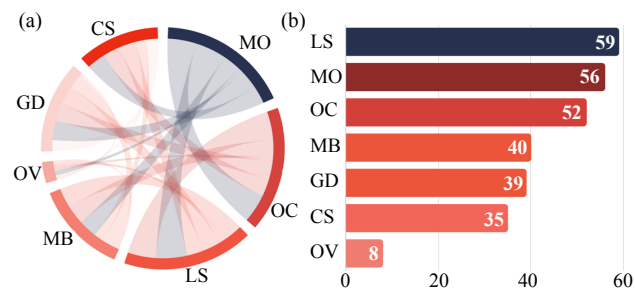


Fig. 6 Attributes statistics. (a)/(b) represent the correlation and frequency of *ASOD60K*'s attributes, respectively.

Tab. 3 Attribute details. General attributes: MO = multiple objects. OC = occlusions. LS = low space. MB = motion blur. 360° geometrical attributes: OV = out-of-view. GD = geometrical distortion. Spatial audio attributes: CS = competing sounds.

Sequence	General				360°		Audio	No.
	MO	OC	LS	MB	OV	GD	CS	
Speaking (35)	French	✓	✓	✓	✓	✓	✓	5
	WaitingRoom	✓	✓	✓	✓	✓	✓	5
	Cooking	✓	✓	✓	✓	✓	✓	5
	AudiIntro	✓	✓	✓	✓	✓	✓	5
	Ellen	✓	✓	✓	✓	✓	✓	5
	GroveAction	✓	✓	✓	✓	✓	✓	5
	Warehouse	✓	✓	✓	✓	✓	✓	5
	GroveConvo	✓	✓	✓	✓	✓	✓	5
	Surfing	✓	✓	✓	✓	✓	✓	5
	Passageway	✓	✓	✓	✓	✓	✓	5
	RuralDriving	✓	✓	✓	✓	✓	✓	5
	Lawn	✓	✓	✓	✓	✓	✓	5
	AudiAd	✓	✓	✓	✓	✓	✓	5
	ScenePlay	✓	✓	✓	✓	✓	✓	5
	UrbanDriving	✓	✓	✓	✓	✓	✓	5
	Interview	✓	✓	✓	✓	✓	✓	5
	Telephone	✓	✓	✓	✓	✓	✓	5
	Walking	✓	✓	✓	✓	✓	✓	5
	Bridge	✓	✓	✓	✓	✓	✓	5
	Breakfast	✓	✓	✓	✓	✓	✓	5
	Debate	✓	✓	✓	✓	✓	✓	5
	BadmintonConvo	✓	✓	✓	✓	✓	✓	5
	Director	✓	✓	✓	✓	✓	✓	5
	ChineseAd	✓	✓	✓	✓	✓	✓	5
	Exhibition	✓	✓	✓	✓	✓	✓	5
	PianoConvo	✓	✓	✓	✓	✓	✓	5
	FilmingSite	✓	✓	✓	✓	✓	✓	5
	Brothers	✓	✓	✓	✓	✓	✓	5
	Rap	✓	✓	✓	✓	✓	✓	5
	Spanish	✓	✓	✓	✓	✓	✓	5
	Questions	✓	✓	✓	✓	✓	✓	5
	PianoMono	✓	✓	✓	✓	✓	✓	5
	Snowfield	✓	✓	✓	✓	✓	✓	5
	Melodrama	✓	✓	✓	✓	✓	✓	5
	Gymnasium	✓	✓	✓	✓	✓	✓	5
Music (16)	Guitar	✓	✓	✓	✓	✓	✓	4
	Subway	✓	✓	✓	✓	✓	✓	4
	Jazz	✓	✓	✓	✓	✓	✓	4
	Bass	✓	✓	✓	✓	✓	✓	4
	Canon	✓	✓	✓	✓	✓	✓	4
	MICOSinging	✓	✓	✓	✓	✓	✓	4
	Clarinet	✓	✓	✓	✓	✓	✓	4
	Trumpet	✓	✓	✓	✓	✓	✓	4
	PianoSaxophone	✓	✓	✓	✓	✓	✓	4
	Chorus	✓	✓	✓	✓	✓	✓	4
	Studio	✓	✓	✓	✓	✓	✓	4
	Church	✓	✓	✓	✓	✓	✓	4
	Duet	✓	✓	✓	✓	✓	✓	4
	Blues	✓	✓	✓	✓	✓	✓	4
	Violins	✓	✓	✓	✓	✓	✓	4
	SingingDancing	✓	✓	✓	✓	✓	✓	4
Miscellanea (16)	Beach	✓	✓	✓	✓	✓	✓	4
	BadmintonGym	✓	✓	✓	✓	✓	✓	4
	InVehicle	✓	✓	✓	✓	✓	✓	4
	Japanese	✓	✓	✓	✓	✓	✓	4
	Tennis	✓	✓	✓	✓	✓	✓	4
	Diesel	✓	✓	✓	✓	✓	✓	4
	Park	✓	✓	✓	✓	✓	✓	4
	Lion	✓	✓	✓	✓	✓	✓	4
	Carriage	✓	✓	✓	✓	✓	✓	4
	Platform	✓	✓	✓	✓	✓	✓	4
	Dog	✓	✓	✓	✓	✓	✓	4
	RacingCar	✓	✓	✓	✓	✓	✓	4
	Train	✓	✓	✓	✓	✓	✓	4
	Football	✓	✓	✓	✓	✓	✓	4
	ParkingLot	✓	✓	✓	✓	✓	✓	4
	Skiing	✓	✓	✓	✓	✓	✓	4
No.	56	52	59	40	8	39	35	289

exclusive geometrical attributes of ER images, and *CS* is a novel attribute attached to audio-visual stimuli (Please see per-video attributes' statistics in Tab. 3).

3.4 Dataset Features and Statistics

Attribute Distribution. The attributes summarize natural daily scenes viewed in omni-direction, also inspire model development for PI-SOD and PV-SOD.

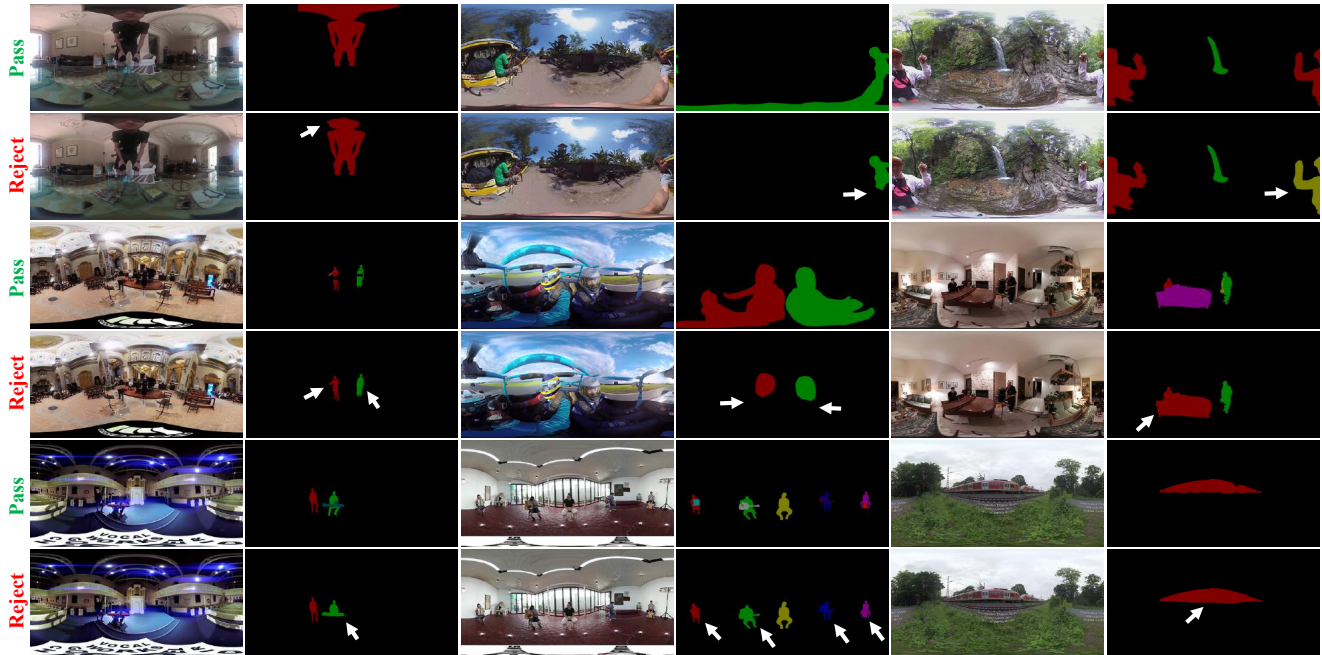


Fig. 7 Passed and rejected examples of annotation quality control.

As shown in Fig. 6, the seven proposed attributes are closely related to each other, representing challenging common scenarios.

Equator Center Bias. Fig. 4 and Fig. 5 visualize the global and super-class center bias [17, 24] of *ASOD60K*. Compared to 360-SOD and 360-SSOD, our dataset shows stronger center bias as it is the only one with salient objects annotated according to participants’ eye fixations, with the starting point set to the center of each video display during the subjective experiments. It has been broadly proved that photographers tend to capture the main content of a 360° video at the equator center, and that users also usually pay more attention to such an area during watching [12, 16, 84]. Our *ASOD60K* is hence more able to reflect real-world viewing behaviors compared to the 360-SOD [46] and 360-SSOD [53].

Instance Size. Following [17], we compute the normalized instances’ size of our *ASOD60K*. The size distribution ranges from 0.03% ~ 23.00%, covering very small objects.

Quality Control. High-quality annotation is one of the most important aspects of training for learning-based models. As illustrated in Fig. 7, we carefully conduct three-fold cross-validation to ensure the annotation quality.

4 Empirical Studies

4.1 Settings

Dataset Splits. All 67 videos are split into separate training and test sets with a random selection strategy, in a ratio of about 6:4. Therefore, we reach a unique split of 40 training and 27 test videos (5,796/4,669 key frames respectively), with corresponding per-pixel instance-/object-level GTs. The testing set is further divided into test0/test1/test2 with 6/6/15 videos, respectively, according to super-class labels (*i.e.*, Miscellanea/Music/Speaking).

Metrics. We apply three widely used SOD metrics to quantitatively compare the SOTA I-SOD/V-SOD models. These metrics include structural measure (S-Measure, S_α) [4, 6], maximum enhanced-alignment measure (E-Measure, E_ϕ) [18, 19] and mean absolute error (MAE) [57]. The MAE [57] focuses on the local (per-pixel) match between ground truth and prediction, while S-Measure (S_α) [4] pays attention to the object structure similarities. Besides, E-Measure (E_ϕ) [18] considers both the local and global information.

MAE computes the mean absolute error between the ground truth $G \in \{0, 1\}$ and a normalized predicted saliency map $P \in [0, 1]$, *i.e.*,

$$MAE = \frac{1}{W \times H} \sum_{i=1}^W \sum_{j=1}^H |G(i, j) - P(i, j)|, \quad (1)$$

where H and W denotes height and width, respectively.

Tab. 4 Performance comparison of 7/3 state-of-the-art conventional I-SOD/V-SOD methods and one PI-SOD method [34] over *ASOD60K*. \uparrow/\downarrow denotes a larger/smaller value is better. Best result of each column is **bolded**.

Type	Publication	Methods	Miscellanea (Test0)			Music (Test1)			Speaking (Test2)		
			$S_\alpha \uparrow$	$E_\phi \uparrow$	$\mathcal{M} \downarrow$	$S_\alpha \uparrow$	$E_\phi \uparrow$	$\mathcal{M} \downarrow$	$S_\alpha \uparrow$	$E_\phi \uparrow$	$\mathcal{M} \downarrow$
I-SOD	CVPR'19	CPD [82]	0.654	0.584	0.035	0.608	0.823	0.018	0.588	0.756	0.026
	ICCV'19	SCRN [83]	0.665	0.564	0.046	0.683	0.841	0.023	0.636	0.739	0.034
	AAAI'20	F3Net [39]	0.655	0.557	0.040	0.662	0.801	0.021	0.626	0.716	0.027
	CVPR'20	MINet [55]	0.650	0.557	0.050	0.670	0.789	0.020	0.590	0.680	0.053
	CVPR'20	LDF [80]	0.663	0.557	0.044	0.671	0.828	0.023	0.625	0.761	0.037
	ECCV'20	CSF [29]	0.652	0.575	0.033	0.665	0.833	0.018	0.636	0.791	0.026
	ECCV'20	GateNet [99]	0.677	0.596	0.044	0.673	0.852	0.018	0.633	0.739	0.034
V-SOD	CVPR'19	COSNet [52]	0.610	0.535	0.031	0.577	0.825	0.016	0.572	0.722	0.023
	ICCV'19	RCRNet [87]	0.661	0.576	0.034	0.695	0.839	0.019	0.632	0.775	0.030
	AAAI'20	PCSA [30]	0.602	0.549	0.034	0.655	0.764	0.021	0.572	0.679	0.026
PI-SOD	SPL'20	FANet [34]	0.610	0.513	0.030	0.646	0.814	0.018	0.566	0.696	0.027

Tab. 5 Performance comparison of 7/3/1 state-of-the-art I-SOD/V-SOD/PI-SOD methods based on each of the attributes.

Attr.	Metrics	I-SOD							V-SOD			PI-SOD
		CPD [82]	SCRN [83]	F3Net [39]	MINet [55]	LDF [80]	CSF [29]	GateNet [99]	COSNet [52]	RCRNet [87]	PCSA [30]	FANet [34]
MO	$S_\alpha \uparrow$	0.610	0.657	0.644	0.624	0.648	0.649	0.653	0.588	0.661	0.606	0.605
	$E_\phi \uparrow$	0.741	0.740	0.702	0.691	0.742	0.752	0.733	0.722	0.746	0.681	0.695
	$\mathcal{M} \downarrow$	0.027	0.034	0.030	0.045	0.033	0.027	0.034	0.024	0.029	0.027	0.025
OC	$S_\alpha \uparrow$	0.606	0.655	0.641	0.619	0.645	0.645	0.650	0.577	0.652	0.599	0.593
	$E_\phi \uparrow$	0.772	0.768	0.725	0.699	0.771	0.780	0.755	0.744	0.763	0.704	0.720
	$\mathcal{M} \downarrow$	0.023	0.029	0.026	0.043	0.028	0.023	0.030	0.020	0.025	0.024	0.022
LS	$S_\alpha \uparrow$	0.605	0.649	0.639	0.618	0.637	0.644	0.647	0.585	0.650	0.609	0.598
	$E_\phi \uparrow$	0.721	0.723	0.693	0.665	0.719	0.740	0.715	0.697	0.723	0.674	0.669
	$\mathcal{M} \downarrow$	0.025	0.034	0.028	0.045	0.037	0.025	0.033	0.022	0.029	0.026	0.025
MB	$S_\alpha \uparrow$	0.622	0.651	0.630	0.620	0.646	0.638	0.645	0.582	0.642	0.586	0.587
	$E_\phi \uparrow$	0.728	0.718	0.692	0.675	0.717	0.749	0.701	0.709	0.734	0.702	0.688
	$\mathcal{M} \downarrow$	0.021	0.029	0.027	0.047	0.029	0.021	0.030	0.019	0.024	0.022	0.020
OV	$S_\alpha \uparrow$	0.634	0.661	0.568	0.633	0.636	0.636	0.639	0.582	0.630	0.600	0.611
	$E_\phi \uparrow$	0.844	0.786	0.571	0.711	0.854	0.837	0.841	0.817	0.848	0.700	0.820
	$\mathcal{M} \downarrow$	0.018	0.021	0.029	0.038	0.039	0.021	0.025	0.021	0.029	0.021	0.018
GD	$S_\alpha \uparrow$	0.630	0.662	0.639	0.633	0.659	0.646	0.658	0.588	0.651	0.578	0.599
	$E_\phi \uparrow$	0.680	0.690	0.641	0.666	0.672	0.695	0.684	0.662	0.695	0.655	0.657
	$\mathcal{M} \downarrow$	0.037	0.042	0.040	0.045	0.043	0.035	0.042	0.032	0.037	0.036	0.034
CS	$S_\alpha \uparrow$	0.625	0.680	0.667	0.654	0.664	0.670	0.676	0.592	0.680	0.620	0.616
	$E_\phi \uparrow$	0.748	0.759	0.712	0.718	0.747	0.745	0.762	0.722	0.736	0.689	0.710
	$\mathcal{M} \downarrow$	0.029	0.035	0.031	0.035	0.034	0.028	0.033	0.026	0.030	0.029	0.028

S-Measure evaluates the structure similarities between salient objects in GT foreground maps and predicted saliency maps:

$$S_\alpha = \alpha \times S_o + (1 - \alpha) \times S_r. \quad (2)$$

where S_o and S_r denotes the object-/region-based structure similarities, respectively. $\alpha \in [0, 1]$ is set as 0.5 so that equal weights are assigned to both the object-level and region-level assessments [4].

E-Measure is a cognitive vision-inspired metric to evaluate both the local and global similarities between two binary maps. Specifically, it is defined as:

$$E_\phi = \frac{1}{W \times H} \sum_{i=1}^W \sum_{j=1}^H \phi_s(i, j), \quad (3)$$

where $\phi_s(i, j)$ represents the enhanced alignment matrix [18].

Training Protocols. To provide a comprehensive benchmark, we collect the released codes of 10 SOTA I-SOD/V-SOD methods and one PI-SOD model, re-train these models with the training set of *ASOD60K* and

the widely used I-SOD training set, DUTS-train [75] (except for FANet [34], which is designed for ER images only). The selected baselines (CPD[82], SCRN[83], F3Net[39], MINet[55], LDF[80], CSF+Res2Net[29], GateNet [99], RCRNet[87], COSNet[52] and PCSA [30]) meet the following criteria: i) classical architectures, ii) recently published and open-sourced, iii) achieve SOTA performance on existing I-SOD/V-SOD benchmarks. Note that all the baselines are trained with the recommended parameter settings.

5 Discussion

From the benchmark results, we observe that, generally, the I-SOD models gain comparable performance to their V-SOD counterparts. One possible reason is that, since the annotations of our *ASOD60K* are only based on key frames, the relatively sparse spatiotemporal information may prevent the V-SOD models from acquiring full performance. In contrast, the visual cues are easily learned by the

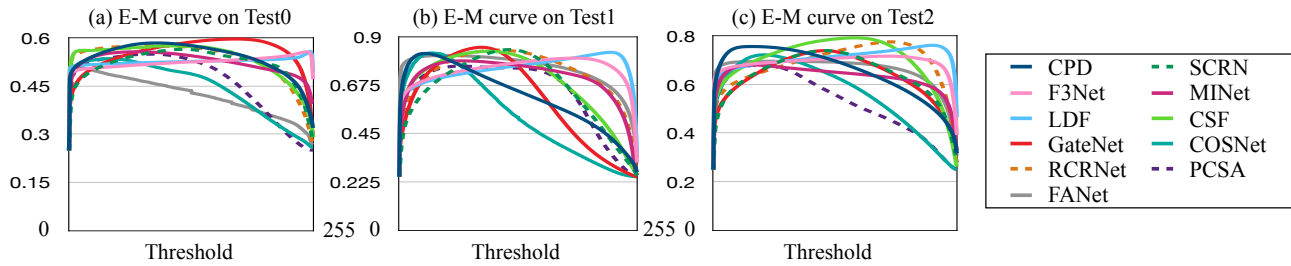


Fig. 8 E-Measure (E-M) curves of all baselines upon our *ASOD60K*.

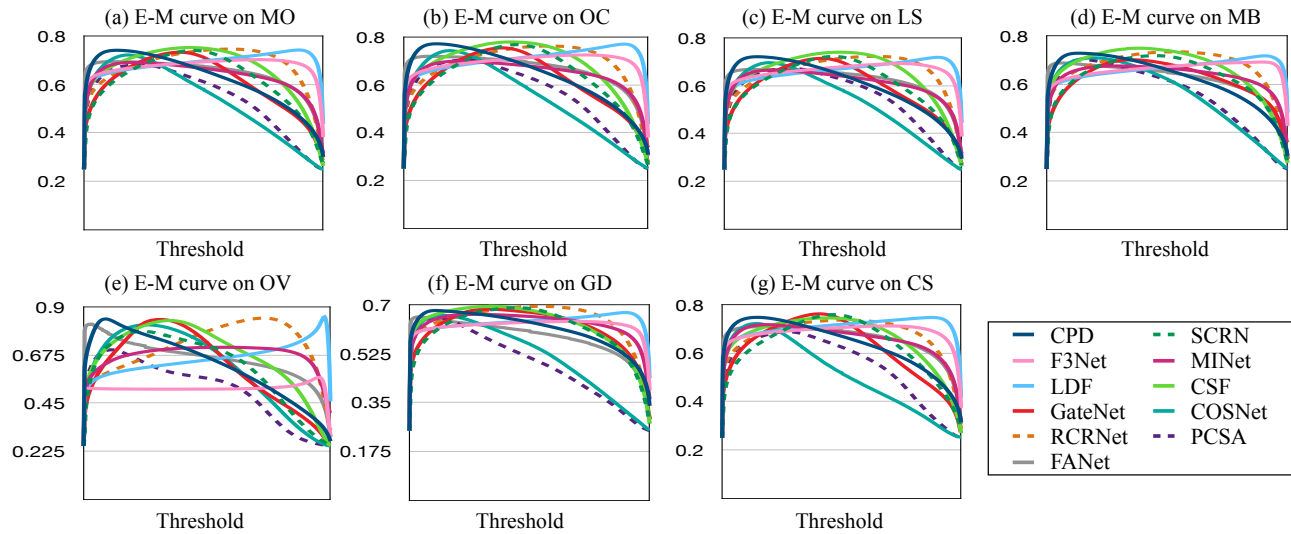


Fig. 9 Attribute-based E-Measure (E-M) curves of all baselines upon our *ASOD60K*.

I-SOD model with such sparsely labeled data.

Overall Performance. From the evaluation in Tab. 4, we observe that, in most cases, the I-SOD methods (*e.g.*, GateNet, and CSF) achieve better performance than the V-SOD (*e.g.*, COSNet, RCRNet, and PCSA) and PI-SOD models. For specific scenes (*e.g.*, speaking), however, SCRN obtains a very competitive performance to GateNet, while performs worse than CSF. The E-Measure performances are shown in Fig. 8.

Attribute Performance. To provide deeper insights for the challenging cases, we report the performances of all 11 baselines on our seven attributes. A detailed attributes-based E-Measure is shown in Fig. 9. As shown in Tab. 5, the average S_α score among the models for the different attributes are: 0.631 (MO), 0.626 (OC), 0.626 (LS), 0.623 (MB), 0.621 (OV), 0.631 (GD) and 0.649 (CS). *Out-of-view* (OV) is the most challenging attribute as the objects usually appear in the corner of the ER images. Besides, the scores on all attributes are less than 0.65, demonstrating the strong challenge of our *ASOD60K* and leaving large room for future improvement.

General Attributes. As shown in Table 3, every

collected video owns at least one general attributes (*i.e.*, *multiple objects (MO)*, *occlusions (OC)*, *motion blur (MB)* and *low space (LS)*), indicating that our *ASOD60K* contains the main challenges faced in so many computer vision fields, such as object detection, video object segmentation, etc. It is worth mentioning that, as the 360° image captures a wide field-of-view (FoV) with the range of $360^\circ \times 180^\circ$, salient objects far from the panoramic camera may perform extremely small sizes, making the *LS* a more challenging situation

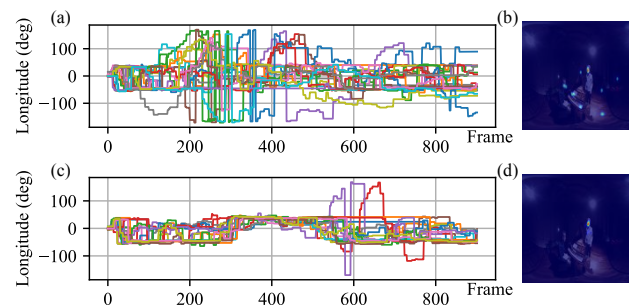


Fig. 10 Eye fixation distributions of all participants watching *PianoConvo* sequence without (a)/with (c) audio. Corresponding fixations are overlaid in (b) and (d), respectively.

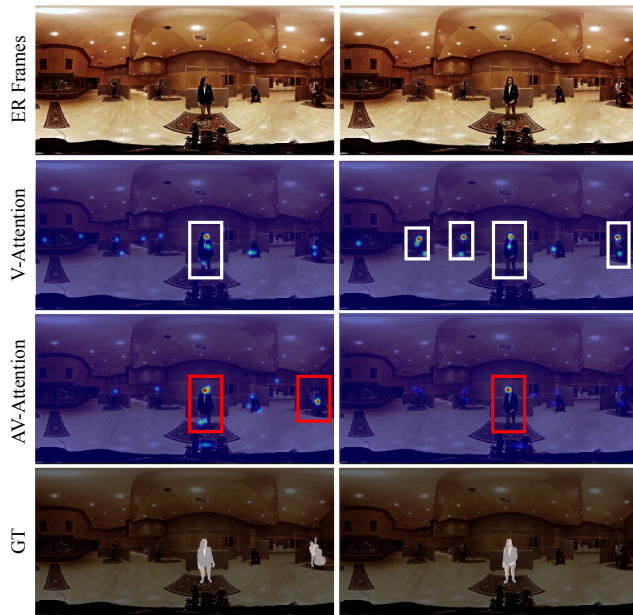


Fig. 11 Visual comparison of visual and audio-visual attention. The objects with high saliency values ($\geq 50\%$) are marked with white/red bounding boxes. Zoom in for details.

within PV-SOD.

Eye Fixations With/Without Audio. Fig. 10 shows an example of 20 participants watching videos without and with audio in longitude, respectively. We find that the eye fixation recordings with audio are highly consistent across subjects, while the recordings without audio are not. Fig. 11 highlights this finding by vividly showing a significant divergence between human attentions (converging/scattering) with and without the guidance of audio information, respectively. Both the quantitative (Fig. 10) and qualitative (Fig. 11) experimental results indicate that human attention highly depends on a co-guidance of audio-visual information.

Audio-Induced Attributes. Creating realistic VR experiences requires 360° videos to be captured with their surrounding visual and audio stimuli. The audio cue plays a significant role in informing the viewers about the location of sounding salient objects in the 360° environment [73], providing an immersive multimedia experience. As shown in Figure 13, the ground truths (GTs) of our videos (especially for those attached with attribute-*competing sounds*) may be largely influenced by the audio cues (*e.g.*, silent visual salient objects are sometimes regarded as non-salient objects in our case, for they are unable to gain a majority of the observers' attention in an acoustic environment), thus being very different when compared with the GTs of existing mute-modal V-SOD datasets

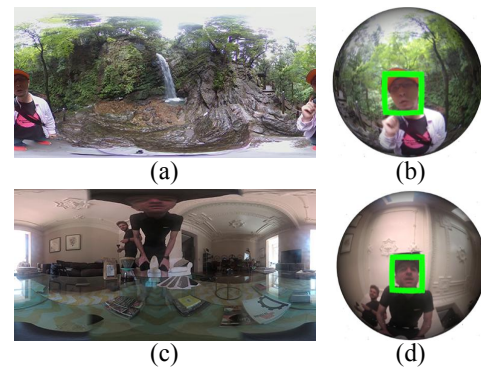


Fig. 12 An illustration of typical geometrical attributes. (a) Out-of-view (OV) in equirectangular (ER) image. (b) OV in spherical field-of-view (FoV). (c) Geometrical distortion (GD) in ER image. (d) GD in spherical FoV.

where visual cues are the only evidence. As shown in Figure 13, most of the baselines tend to detect all visual salient objects while ignore the audio-visual attention shifts among the key frames. It is necessary for future works to model both the visual and audio cue for a better performance on our *ASOD60K*.

360° Geometrical Attributes. The 360° image captures a scene covering omnidirectional ($360^\circ \times 180^\circ$) spatial information, thus including more comprehensive object structures when compared to 2D image, which owns a FoV with limited range. For instance, as shown in Figure 12, the *out-of-view (OV)* object in equirectangular (ER) image has a well shape when re-projected to a specific FoV on sphere. However, *OV* objects in 2D images or videos permanently lose spatial information due to the limited viewing range of the normal cameras. *Geometrical distortion (GD)* is the other important attribute of 360° images under ER projection (Figure 12 (c)), which is largely alleviated in spherical FoV (Figure 12 (d)). As there is no perfect 2D (planar) representation for 360° images, a trade-off between geometrical distorted extent and spatial information retention will always exist. Future methods may take advantage of multiple projection methods for improved performance when conducting PV-SOD.

Small Objects. We define small objects *LS* (Tab. 2) as those that occupy an area smaller than 0.5% of the whole image. *LS*, as one of the well-known challenges in the image segmentation task, is still not completely solved. As stated in Sec. 3.4, due to the wide FoV range of $360^\circ \times 180^\circ$, the smallest object in our *ASOD60K* only occupies 0.03% of the ER image, making it more challenging. As for the attribute-based performance, we observe that models under this situation achieve a comparable performance to the others. However,

considering that the applied metrics may be biased toward the true negative, the true positive score tends to be worse than the existing shown performance.

Novel Metric. In this benchmark, we only introduce widely used metrics for I-SOD. However, PV-SOD involves context (*e.g.*, audio, spatial and temporal) relationship between salient/non-salient objects, which is quite important for PV-SOD assessment. Thus, designing a more suitable evaluation metric for PV-SOD is an interesting and open issue.

Future Directions. Currently, we only focus on the object-level task. However, the instance-level task is more difficult and may be suitable for many image-editing applications. In addition, as described in [17], studying non-salient objects will provide rich context for reasoning the salient objects in a scene. Besides, in this study, we only provide sparse annotations for the proposed dataset. However, dense annotations like those given in DAVIS [58] dataset can provide more valuable information (*e.g.*, sequence-to-sequence modeling or audio-visual matching) for both traditional I-SOD and PV-SOD models. Finally, based on the findings of significant differences between visual and audio-visual saliency attributes as illustrated in “Audio-Induced Attributes” of Section Discussion, we find that an absence of audio cues may significantly limit current SOD models from acquiring their best performance on *ASOD60K*. Future researches may focus more on utilizing the audio cues for better object-level saliency detection in panoramic scenes.

6 Conclusion

We have proposed *ASOD60K*, the first large-scale dataset for the PV-SOD task. Compared with the traditional SOD task, PV-SOD is more challenging. The hierarchical annotations enable *ASOD60K* to easily be extended to different-level tasks, such as weakly supervised learning, multi-modality learning, and head movement/fixation prediction. In addition, we provide several empirical rules for creating high-quality datasets. We have further investigated 11 cutting-edge methods at both the overall and attribute levels. The obtained findings indicate that PV-SOD is far from being solved. We hope that our studies will facilitate SOD research towards panoramic videos and thus inspiring more novel ideas for AR/VR applications.

Appendix

Per Video Performance & Visual Results. The per-video quantitative results are shown in Tab. 6 and

Tab. 7. Please refer to Fig. 14, Fig. 15 and Fig. 16 for visual results.

References

- [1] A. Borji, M.-M. Cheng, Q. Hou, H. Jiang, and J. Li. Salient object detection: A survey. *CVMJ*, 5(2):117–150, 2019.
- [2] A. Borji, M.-M. Cheng, H. Jiang, and J. Li. Salient object detection: A benchmark. *IEEE TIP*, 24(12):5706–5722, 2015.
- [3] F.-Y. Chao, C. Ozcinar, C. Wang, E. Zerman, L. Zhang, W. Hamidouche, O. Deforges, and A. Smolic. Audio-visual perception of omnidirectional video for virtual reality applications. In *IEEE ICMEW*, pages 1–6, 2020.
- [4] M.-M. Chen and D.-P. Fan. Structure-measure: A new way to evaluate foreground maps. *IJCV*, 2021.
- [5] H.-T. Cheng, C.-H. Chao, J.-D. Dong, H.-K. Wen, T.-L. Liu, and M. Sun. Cube padding for weakly-supervised saliency prediction in 360 videos. In *IEEE CVPR*, pages 1420–1429, 2018.
- [6] M.-M. Cheng and D.-P. Fan. Structure-measure: A new way to evaluate foreground maps. *IJCV*, 2021.
- [7] S.-H. Chou, C. Sun, W.-Y. Chang, W.-T. Hsu, M. Sun, and J. Fu. 360-indoor: Towards learning real-world objects in 360deg indoor equirectangular images. In *IEEE WACV*, pages 845–853, 2020.
- [8] T. S. Cohen, M. Geiger, J. Köhler, and M. Welling. Spherical cnns. *ICLR*, 2018.
- [9] T. S. Cohen, M. Weiler, B. Kicanaoglu, and M. Welling. Gauge equivariant convolutional networks and the icosahedral cnn. *ICML*, 2019.
- [10] B. Coors, A. Paul Condurache, and A. Geiger. Spherenet: Learning spherical representations for detection and classification in omnidirectional images. In *ECCV*, pages 518–533, 2018.
- [11] X. Corbillon, F. De Simone, and G. Simon. 360-degree video head movement dataset. In *ACM MMSys*, pages 199–204, 2017.
- [12] E. J. David, J. Gutiérrez, A. Coutrot, M. P. Da Silva, and P. L. Callet. A dataset of head and eye movements for 360 videos. In *ACM MMSys*, pages 432–437, 2018.
- [13] J. Deng, W. Dong, R. Socher, L.-J. Li, K. Li, and L. Fei-Fei. Imagenet: A large-scale hierarchical image database. In *IEEE CVPR*, pages 248–255, 2009.
- [14] M. Eder, M. Shvets, J. Lim, and J.-M. Frahm. Tangent images for mitigating spherical distortion. In *IEEE CVPR*, pages 12426–12434, 2020.
- [15] C. Esteves, C. Allen-Blanchette, A. Makadia, and K. Daniilidis. Learning so (3) equivariant representations with spherical cnns. In *ECCV*, pages 52–68, 2018.
- [16] C.-L. Fan, W.-C. Lo, Y.-T. Pai, and C.-H. Hsu. A survey on 360 video streaming: Acquisition, transmission, and display. *ACM Computing Surveys*, 52(4):1–36, 2019.
- [17] D.-P. Fan, M.-M. Cheng, J.-J. Liu, S.-H. Gao, Q. Hou, and A. Borji. Salient objects in clutter: Bringing

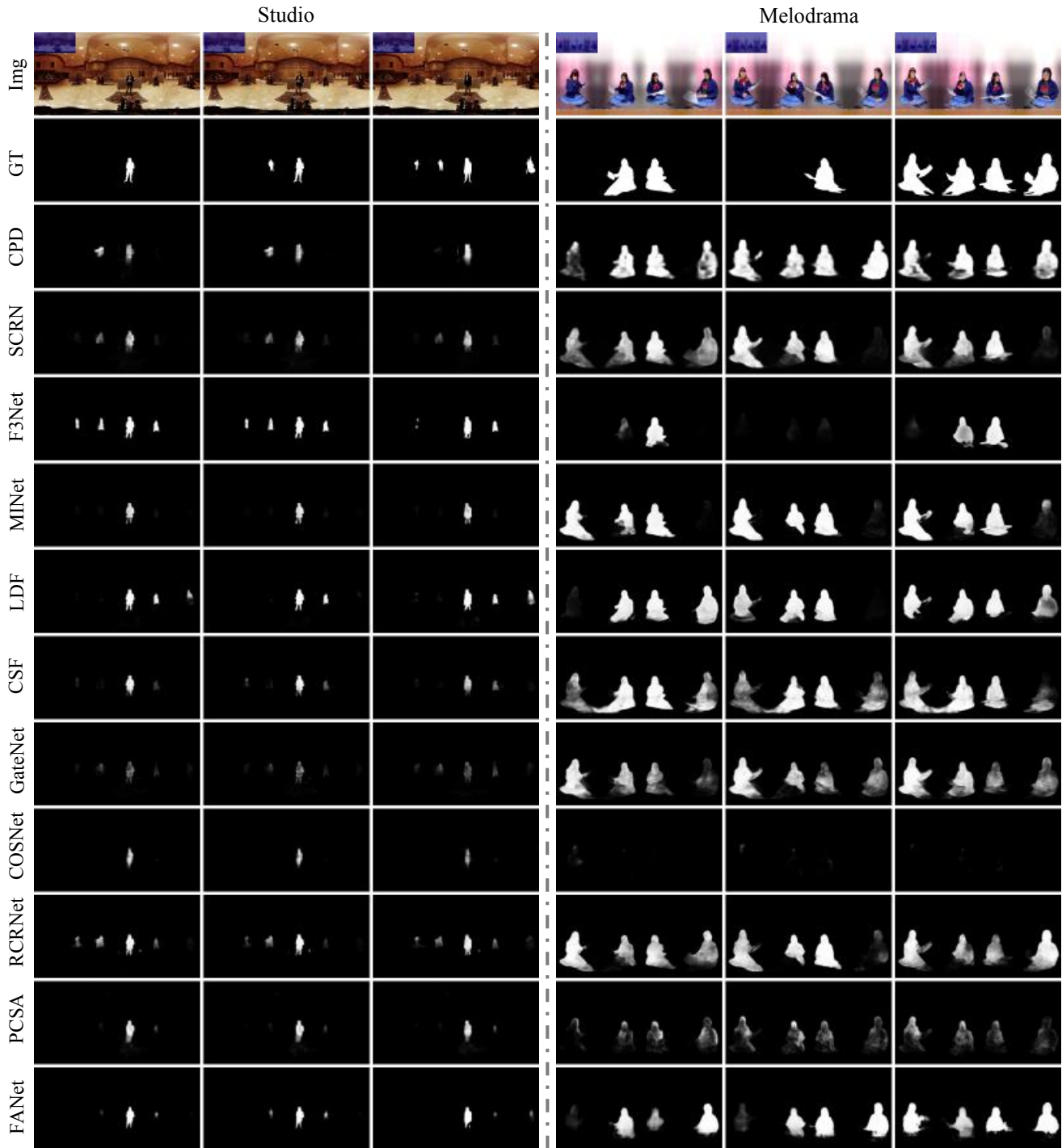


Fig. 13 An illustration of the unique audio-visual attribute, competing sounds. Img = image. GT = ground truth.

salient object detection to the foreground. In *ECCV*, pages 186–202, 2018.

- [18] D.-P. Fan, C. Gong, Y. Cao, B. Ren, M.-M. Cheng, and A. Borji. Enhanced-alignment measure for binary foreground map evaluation. In *IJCAI*, pages 698–704, 2018.
- [19] D.-P. Fan, G.-P. Ji, X. Qin, and M.-M. Cheng.

Cognitive vision inspired object segmentation metric and loss function. *SCIENTIA SINICA Informationis*, 6, 2021.

- [20] D.-P. Fan, T. Li, Z. Lin, G.-P. Ji, D. Zhang, M.-M. Cheng, H. Fu, and J. Shen. Re-thinking co-salient object detection. *IEEE TPAMI*, 2021.
- [21] D.-P. Fan, Z. Lin, G.-P. Ji, D. Zhang, H. Fu, and M.-

Tab. 6 Sequence performance comparison of 7/3/1 SOTA I-SOD/V-SOD/PI-SOD methods. Sp. = Speaking. Mu. = Music.

Super-class/Sequence	Metrics	I-SOD							V-SOD			PI-SOD
		CPD [82]	SCRN [83]	F3Net [39]	MINet [55]	LDF [80]	CSF [29]	GateNet [99]	COSNet [52]	RCRNet [87]	PCSA [30]	FANet [34]
Sp./Debate	S_α ↑	0.547	0.620	0.605	0.553	0.566	0.576	0.628	0.514	0.559	0.571	0.557
	max E_ϕ ↑	0.764	0.855	0.854	0.800	0.842	0.853	0.849	0.844	0.843	0.836	0.755
	mean E_ϕ ↑	0.600	0.752	0.818	0.592	0.829	0.802	0.768	0.410	0.809	0.605	0.702
	\mathcal{M} ↓	0.014	0.016	0.014	0.012	0.012	0.013	0.015	0.009	0.013	0.012	0.015
Sp./BadmintonConvo	S_α ↑	0.712	0.669	0.617	0.712	0.613	0.647	0.652	0.613	0.668	0.550	0.635
	max E_ϕ ↑	0.867	0.822	0.611	0.850	0.814	0.826	0.846	0.845	0.804	0.743	0.830
	mean E_ϕ ↑	0.749	0.663	0.555	0.815	0.659	0.662	0.737	0.603	0.773	0.434	0.704
	\mathcal{M} ↓	0.027	0.034	0.032	0.034	0.068	0.033	0.046	0.032	0.039	0.033	0.030
Sp./Director	S_α ↑	0.679	0.753	0.701	0.677	0.756	0.772	0.726	0.716	0.755	0.731	0.672
	max E_ϕ ↑	0.852	0.880	0.891	0.832	0.902	0.900	0.894	0.899	0.883	0.918	0.844
	mean E_ϕ ↑	0.735	0.729	0.852	0.773	0.849	0.810	0.681	0.744	0.774	0.718	0.768
	\mathcal{M} ↓	0.031	0.038	0.032	0.037	0.029	0.028	0.034	0.029	0.037	0.031	0.030
Sp./ChineseAd	S_α ↑	0.601	0.645	0.551	0.477	0.631	0.630	0.605	0.553	0.542	0.569	0.595
	max E_ϕ ↑	0.895	0.883	0.908	0.695	0.906	0.908	0.913	0.910	0.899	0.910	0.850
	mean E_ϕ ↑	0.483	0.524	0.527	0.391	0.576	0.635	0.544	0.641	0.632	0.470	0.502
	\mathcal{M} ↓	0.009	0.009	0.042	0.069	0.027	0.011	0.012	0.015	0.028	0.010	0.007
Sp./Exhibition	S_α ↑	0.487	0.469	0.480	0.469	0.428	0.492	0.486	0.487	0.473	0.510	0.475
	max E_ϕ ↑	0.614	0.658	0.605	0.597	0.689	0.770	0.735	0.811	0.576	0.773	0.560
	mean E_ϕ ↑	0.486	0.365	0.460	0.350	0.270	0.508	0.459	0.514	0.349	0.512	0.329
	\mathcal{M} ↓	0.013	0.061	0.009	0.042	0.139	0.011	0.013	0.008	0.040	0.014	0.024
Sp./PianoConvo	S_α ↑	0.577	0.652	0.579	0.607	0.639	0.636	0.586	0.603	0.718	0.509	0.632
	max E_ϕ ↑	0.871	0.851	0.847	0.875	0.880	0.858	0.885	0.888	0.880	0.882	0.863
	mean E_ϕ ↑	0.774	0.673	0.745	0.833	0.847	0.807	0.693	0.706	0.803	0.420	0.804
	\mathcal{M} ↓	0.037	0.035	0.035	0.038	0.033	0.036	0.036	0.035	0.028	0.033	0.033
Sp./FilmingSite	S_α ↑	0.578	0.633	0.603	0.610	0.637	0.645	0.636	0.578	0.640	0.633	0.522
	max E_ϕ ↑	0.727	0.762	0.681	0.766	0.799	0.766	0.787	0.708	0.738	0.805	0.793
	mean E_ϕ ↑	0.562	0.627	0.626	0.636	0.707	0.654	0.613	0.540	0.628	0.652	0.727
	\mathcal{M} ↓	0.013	0.023	0.023	0.030	0.017	0.014	0.020	0.012	0.013	0.017	0.016
Sp./Brothers	S_α ↑	0.673	0.686	0.638	0.655	0.652	0.697	0.685	0.662	0.664	0.666	0.623
	max E_ϕ ↑	0.778	0.806	0.747	0.772	0.746	0.816	0.792	0.784	0.813	0.820	0.729
	mean E_ϕ ↑	0.688	0.677	0.713	0.705	0.706	0.715	0.629	0.661	0.728	0.650	0.681
	\mathcal{M} ↓	0.018	0.024	0.023	0.024	0.025	0.017	0.022	0.015	0.019	0.016	0.016
Sp./Rap	S_α ↑	0.498	0.477	0.521	0.343	0.507	0.525	0.463	0.482	0.506	0.495	0.532
	max E_ϕ ↑	0.830	0.816	0.831	0.471	0.814	0.824	0.761	0.828	0.858	0.832	0.818
	mean E_ϕ ↑	0.530	0.387	0.548	0.260	0.484	0.678	0.400	0.513	0.590	0.566	0.733
	\mathcal{M} ↓	0.006	0.087	0.021	0.371	0.025	0.012	0.095	0.007	0.020	0.009	0.009
Sp./Spanish	S_α ↑	0.606	0.765	0.746	0.679	0.793	0.713	0.701	0.724	0.700	0.543	0.602
	max E_ϕ ↑	0.838	0.870	0.851	0.819	0.873	0.854	0.865	0.877	0.862	0.839	0.728
	mean E_ϕ ↑	0.651	0.807	0.835	0.727	0.865	0.797	0.822	0.784	0.800	0.486	0.503
	\mathcal{M} ↓	0.038	0.030	0.032	0.035	0.025	0.036	0.040	0.032	0.037	0.042	0.035
Sp./Questions	S_α ↑	0.505	0.640	0.740	0.563	0.605	0.691	0.671	0.576	0.676	0.595	0.549
	max E_ϕ ↑	0.925	0.921	0.901	0.926	0.920	0.915	0.922	0.935	0.907	0.909	0.757
	mean E_ϕ ↑	0.763	0.609	0.870	0.576	0.855	0.700	0.574	0.569	0.667	0.540	0.703
	\mathcal{M} ↓	0.009	0.011	0.006	0.007	0.010	0.010	0.009	0.009	0.014	0.012	0.013
Sp./PianoMono	S_α ↑	0.598	0.555	0.573	0.572	0.629	0.522	0.637	0.506	0.611	0.502	0.502
	max E_ϕ ↑	0.702	0.855	0.766	0.796	0.861	0.842	0.755	0.859	0.831	0.796	0.715
	mean E_ϕ ↑	0.682	0.736	0.688	0.739	0.746	0.758	0.696	0.500	0.736	0.397	0.633
	\mathcal{M} ↓	0.057	0.054	0.044	0.056	0.054	0.048	0.060	0.039	0.047	0.037	0.043
Sp./Snowfield	S_α ↑	0.729	0.811	0.778	0.800	0.819	0.779	0.823	0.601	0.794	0.580	0.578
	max E_ϕ ↑	0.739	0.816	0.741	0.784	0.819	0.763	0.836	0.864	0.779	0.812	0.775
	mean E_ϕ ↑	0.677	0.778	0.720	0.764	0.792	0.716	0.788	0.485	0.753	0.514	0.618
	\mathcal{M} ↓	0.032	0.029	0.031	0.028	0.026	0.029	0.027	0.033	0.030	0.035	0.040
Sp./Melodrama	S_α ↑	0.609	0.685	0.655	0.673	0.667	0.664	0.617	0.467	0.608	0.604	0.568
	max E_ϕ ↑	0.782	0.835	0.837	0.811	0.835	0.841	0.816	0.788	0.816	0.831	0.794
	mean E_ϕ ↑	0.699	0.744	0.732	0.773	0.784	0.717	0.710	0.296	0.730	0.521	0.770
	\mathcal{M} ↓	0.108	0.084	0.068	0.083	0.079	0.095	0.100	0.076	0.100	0.079	0.098
Sp./Gymnasium	S_α ↑	0.551	0.514	0.492	0.501	0.501	0.507	0.537	0.506	0.520	0.503	0.505
	max E_ϕ ↑	0.806	0.683	0.830	0.700	0.813	0.686	0.754	0.863	0.760	0.798	0.752
	mean E_ϕ ↑	0.584	0.545	0.461	0.593	0.469	0.512	0.487	0.584	0.518	0.468	0.642
	\mathcal{M} ↓	0.007	0.013	0.021	0.011	0.020	0.016	0.020	0.007	0.017	0.027	0.010
Mu./Studio	S_α ↑	0.741	0.770	0.753	0.788	0.758	0.739	0.724	0.637	0.778	0.756	0.760
	max E_ϕ ↑	0.878	0.889	0.898	0.904	0.892	0.899	0.891	0.904	0.893	0.901	0.895
	mean E_ϕ ↑	0.745	0.731	0.832	0.826	0.847	0.756	0.601	0.629	0.800	0.729	0.859
	\mathcal{M} ↓	0.008	0.009	0.010	0.006	0.009	0.009	0.010	0.008	0.009	0.008	0.007

M. Cheng. Taking a deeper look at co-salient object detection. In *IEEE CVPR*, pages 2919–2929, 2020.

- [22] D.-P. Fan, Z. Lin, Z. Zhang, M. Zhu, and M.-M. Cheng. Rethinking rgb-d salient object detection: Models, data sets, and large-scale benchmarks. *IEEE TNNLS*, 2021.
- [23] D.-P. Fan, W. Wang, M.-M. Cheng, and J. Shen. Shifting more attention to video salient object detection. In *IEEE CVPR*, pages 8554–8564, 2019.
- [24] D.-P. Fan, J. Zhang, G. Xu, M.-M. Cheng, and

L. Shao. Salient objects in clutter. *arXiv preprint arXiv:2105.03053*, 2021.

- [25] Q. Fan, D.-P. Fan, H. Fu, C.-K. Tang, L. Shao, and Y.-W. Tai. Group collaborative learning for co-salient object detection. In *IEEE CVPR*, 2021.
- [26] M. Feng, H. Lu, and E. Ding. Attentive feedback network for boundary-aware salient object detection. In *IEEE CVPR*, 2019.
- [27] K. Fu, D.-P. Fan, G.-P. Ji, and Q. Zhao. JI-dcf: Joint learning and densely-cooperative fusion framework for

Tab. 7 Sequence performance comparison of 7/3/1 SOTA I-SOD/V-SOD/PI-SOD methods. Mu. = Music. Mi. = Miscellanea.

Super-class/Sequence	Metrics	I-SOD							V-SOD			PI-SOD
		CPD [82]	SCRN [83]	F3Net [39]	MINet [55]	LDF [80]	CSF [29]	GateNet [99]	COSNet [52]	RCRNet [87]	PCSA [30]	FANet [34]
Mu./Church	S_α ↑	0.527	0.589	0.621	0.566	0.518	0.624	0.651	0.562	0.676	0.623	0.679
	max E_ϕ ↑	0.868	0.917	0.933	0.747	0.932	0.903	0.950	0.887	0.900	0.942	0.866
	mean E_ϕ ↑	0.451	0.575	0.731	0.576	0.715	0.601	0.657	0.487	0.635	0.577	0.774
	\mathcal{M} ↓	0.007	0.012	0.012	0.021	0.018	0.011	0.008	0.006	0.008	0.018	0.007
Mu./Duet	S_α ↑	0.662	0.704	0.698	0.653	0.751	0.648	0.730	0.553	0.731	0.538	0.643
	max E_ϕ ↑	0.879	0.891	0.892	0.876	0.898	0.903	0.883	0.901	0.889	0.873	0.876
	mean E_ϕ ↑	0.810	0.705	0.792	0.821	0.808	0.693	0.735	0.542	0.776	0.509	0.765
	\mathcal{M} ↓	0.041	0.058	0.044	0.039	0.033	0.033	0.036	0.036	0.033	0.036	0.031
Mu./Blues	S_α ↑	0.580	0.742	0.776	0.722	0.771	0.734	0.740	0.595	0.765	0.743	0.600
	max E_ϕ ↑	0.879	0.889	0.890	0.802	0.871	0.844	0.893	0.884	0.894	0.904	0.852
	mean E_ϕ ↑	0.598	0.688	0.830	0.698	0.789	0.766	0.640	0.473	0.834	0.715	0.612
	\mathcal{M} ↓	0.016	0.015	0.013	0.027	0.015	0.015	0.015	0.015	0.013	0.017	0.014
Mu./Violins	S_α ↑	0.589	0.668	0.537	0.692	0.661	0.631	0.656	0.578	0.669	0.671	0.604
	max E_ϕ ↑	0.852	0.877	0.578	0.861	0.883	0.845	0.872	0.851	0.868	0.856	0.790
	mean E_ϕ ↑	0.649	0.655	0.477	0.775	0.722	0.724	0.569	0.597	0.724	0.625	0.749
	\mathcal{M} ↓	0.017	0.020	0.015	0.016	0.022	0.019	0.017	0.015	0.021	0.020	0.017
Mu./SingingDancing	S_α ↑	0.506	0.601	0.582	0.560	0.561	0.594	0.568	0.521	0.569	0.558	0.557
	max E_ϕ ↑	0.804	0.820	0.815	0.820	0.673	0.782	0.813	0.791	0.810	0.812	0.759
	mean E_ϕ ↑	0.500	0.587	0.758	0.565	0.618	0.589	0.547	0.452	0.637	0.608	0.705
	\mathcal{M} ↓	0.026	0.034	0.037	0.025	0.042	0.026	0.026	0.023	0.030	0.034	0.033
Mi./Dog	S_α ↑	0.497	0.516	0.571	0.560	0.569	0.557	0.562	0.523	0.562	0.539	0.520
	max E_ϕ ↑	0.548	0.685	0.535	0.551	0.593	0.572	0.589	0.671	0.612	0.693	0.345
	mean E_ϕ ↑	0.460	0.457	0.493	0.511	0.424	0.532	0.515	0.494	0.548	0.544	0.325
	\mathcal{M} ↓	0.013	0.015	0.014	0.007	0.020	0.004	0.009	0.005	0.004	0.005	0.003
Mi./RacingCar	S_α ↑	0.770	0.769	0.763	0.770	0.772	0.771	0.791	0.760	0.772	0.755	0.762
	max E_ϕ ↑	0.428	0.438	0.365	0.439	0.459	0.458	0.448	0.449	0.453	0.426	0.285
	mean E_ϕ ↑	0.315	0.338	0.283	0.349	0.332	0.287	0.370	0.276	0.293	0.261	0.260
	\mathcal{M} ↓	0.089	0.115	0.087	0.109	0.102	0.085	0.107	0.083	0.087	0.085	0.081
Mi./Train	S_α ↑	0.604	0.616	0.614	0.607	0.629	0.594	0.663	0.501	0.524	0.515	0.489
	max E_ϕ ↑	0.618	0.700	0.531	0.676	0.589	0.665	0.780	0.556	0.671	0.526	0.432
	mean E_ϕ ↑	0.581	0.553	0.486	0.493	0.554	0.558	0.634	0.351	0.462	0.416	0.386
	\mathcal{M} ↓	0.024	0.030	0.020	0.041	0.012	0.013	0.022	0.016	0.016	0.028	0.016
Mi./Football	S_α ↑	0.653	0.696	0.618	0.656	0.668	0.658	0.676	0.648	0.710	0.635	0.556
	max E_ϕ ↑	0.833	0.856	0.790	0.830	0.835	0.846	0.820	0.811	0.866	0.810	0.742
	mean E_ϕ ↑	0.634	0.676	0.755	0.633	0.770	0.721	0.663	0.649	0.732	0.630	0.477
	\mathcal{M} ↓	0.004	0.004	0.004	0.003	0.004	0.003	0.004	0.003	0.002	0.003	0.002
Mi./ParkingLot	S_α ↑	0.635	0.627	0.624	0.564	0.640	0.562	0.625	0.548	0.624	0.501	0.627
	max E_ϕ ↑	0.666	0.645	0.649	0.614	0.650	0.646	0.663	0.659	0.661	0.622	0.665
	mean E_ϕ ↑	0.641	0.551	0.600	0.597	0.625	0.602	0.610	0.482	0.612	0.501	0.593
	\mathcal{M} ↓	0.028	0.041	0.048	0.059	0.041	0.035	0.045	0.027	0.038	0.029	0.026
Mi./Skiing	S_α ↑	0.697	0.728	0.689	0.727	0.632	0.757	0.695	0.624	0.745	0.641	0.590
	max E_ϕ ↑	0.784	0.764	0.782	0.730	0.829	0.781	0.761	0.814	0.806	0.781	0.744
	mean E_ϕ ↑	0.705	0.645	0.669	0.661	0.517	0.675	0.605	0.573	0.716	0.613	0.500
	\mathcal{M} ↓	0.015	0.024	0.027	0.025	0.044	0.015	0.030	0.014	0.016	0.016	0.012

rgb-d salient object detection. In *IEEE CVPR*, pages 3052–3062, 2020.

- [28] K. Fu, D.-P. Fan, G.-P. Ji, Q. Zhao, J. Shen, and C. Zhu. Siamese network for rgb-d salient object detection and beyond. *IEEE TPAMI*, 2021.
- [29] S.-H. Gao, Y.-Q. Tan, M.-M. Cheng, C. Lu, Y. Chen, and S. Yan. Highly efficient salient object detection with 100k parameters. In *ECCV*, 2020.
- [30] Y. Gu, L. Wang, Z. Wang, Y. Liu, M.-M. Cheng, and S.-P. Lu. Pyramid constrained self-attention network for fast video salient object detection. In *AAAI*, 2020.
- [31] K. He, X. Zhang, S. Ren, and J. Sun. Deep residual learning for image recognition. In *IEEE CVPR*, pages 770–778, 2016.
- [32] H.-N. Hu, Y.-C. Lin, M.-Y. Liu, H.-T. Cheng, Y.-J. Chang, and M. Sun. Deep 360 pilot: Learning a deep agent for piloting through 360 sports videos. In *IEEE CVPR*, pages 1396–1405, 2017.
- [33] H.-N. Hu, Y.-C. Lin, M.-Y. Liu, H.-T. Cheng, Y.-J. Chang, and M. Sun. Deep 360 pilot: Learning a deep agent for piloting through 360 sports videos. In *IEEE CVPR*, pages 1396–1405, 2017.
- [34] M. Huang, Z. Liu, G. Li, X. Zhou, and O. Le Meur. Fanet: Features adaptation network for 360° omnidirectional salient object detection. *IEEE SPL*, 27:1819–1823, 2020.
- [35] S. Jain, P. Yarlagadda, R. Subramanian, and V. Gandhi. Avinet: Diving deep into audio-visual saliency prediction. *arXiv preprint arXiv:2012.06170*, 2020.
- [36] G.-P. Ji, K. Fu, Z. Wu, D.-P. Fan, J. Shen, and L. Shao. Full-duplex strategy for video object segmentation. In *IEEE ICCV*, 2021.
- [37] C. Jiang, J. Huang, K. Kashinath, P. Marcus, M. Niessner, et al. Spherical cnns on unstructured grids. *ICLR*, 2019.
- [38] Y. Jiang, T. Zhou, G.-P. Ji, K. Fu, Q. Zhao, and D.-P. Fan. Light field salient object detection: A review and benchmark. *arXiv preprint arXiv:2010.04968*, 2020.
- [39] Q. H. Jun Wei, Shuhui Wang. F3net: Fusion, feedback

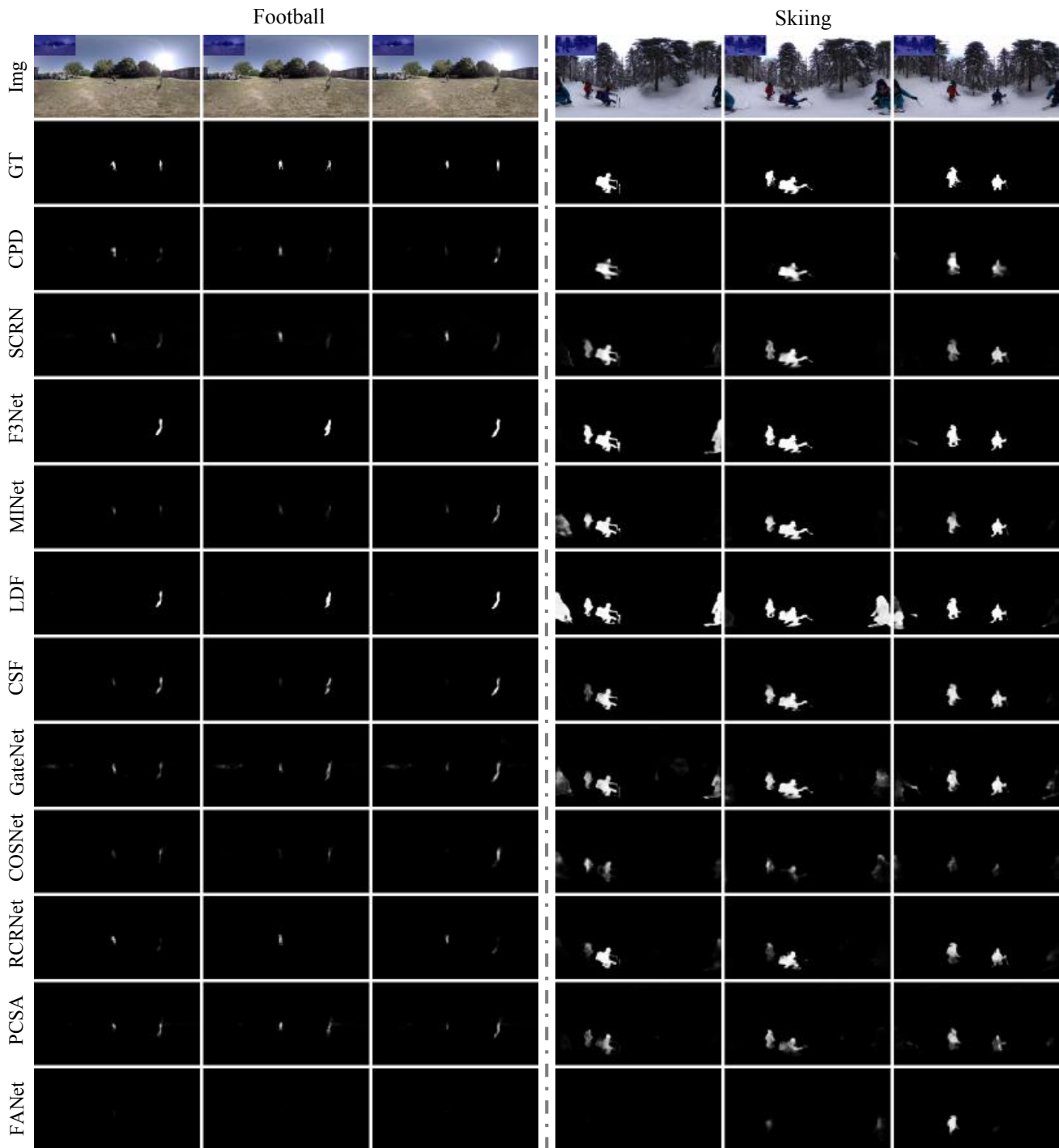


Fig. 14 Visual results of all baselines on the *ASOD60K-test0* (Miscellanea). Img = image. GT = ground truth.

- and focus for salient object detection. In *AAAI*, 2020.
- [40] H. Kim, Y. Kim, J.-Y. Sim, and C.-S. Kim. Spatiotemporal saliency detection for video sequences based on random walk with restart. *IEEE TIP*, 24(8):2552–2564, 2015.
- [41] F. Li, T. Kim, A. Humayun, D. Tsai, and J. M. Rehg. Video segmentation by tracking many figure-ground

- segments. In *IEEE ICCV*, pages 2192–2199, 2013.
- [42] G. Li, Y. Xie, L. Lin, and Y. Yu. Instance-level salient object segmentation. In *IEEE CVPR*, pages 2386–2395, 2017.
- [43] G. Li, Y. Xie, T. Wei, K. Wang, and L. Lin. Flow guided recurrent neural encoder for video salient object detection. In *IEEE CVPR*, pages 3243–3252,

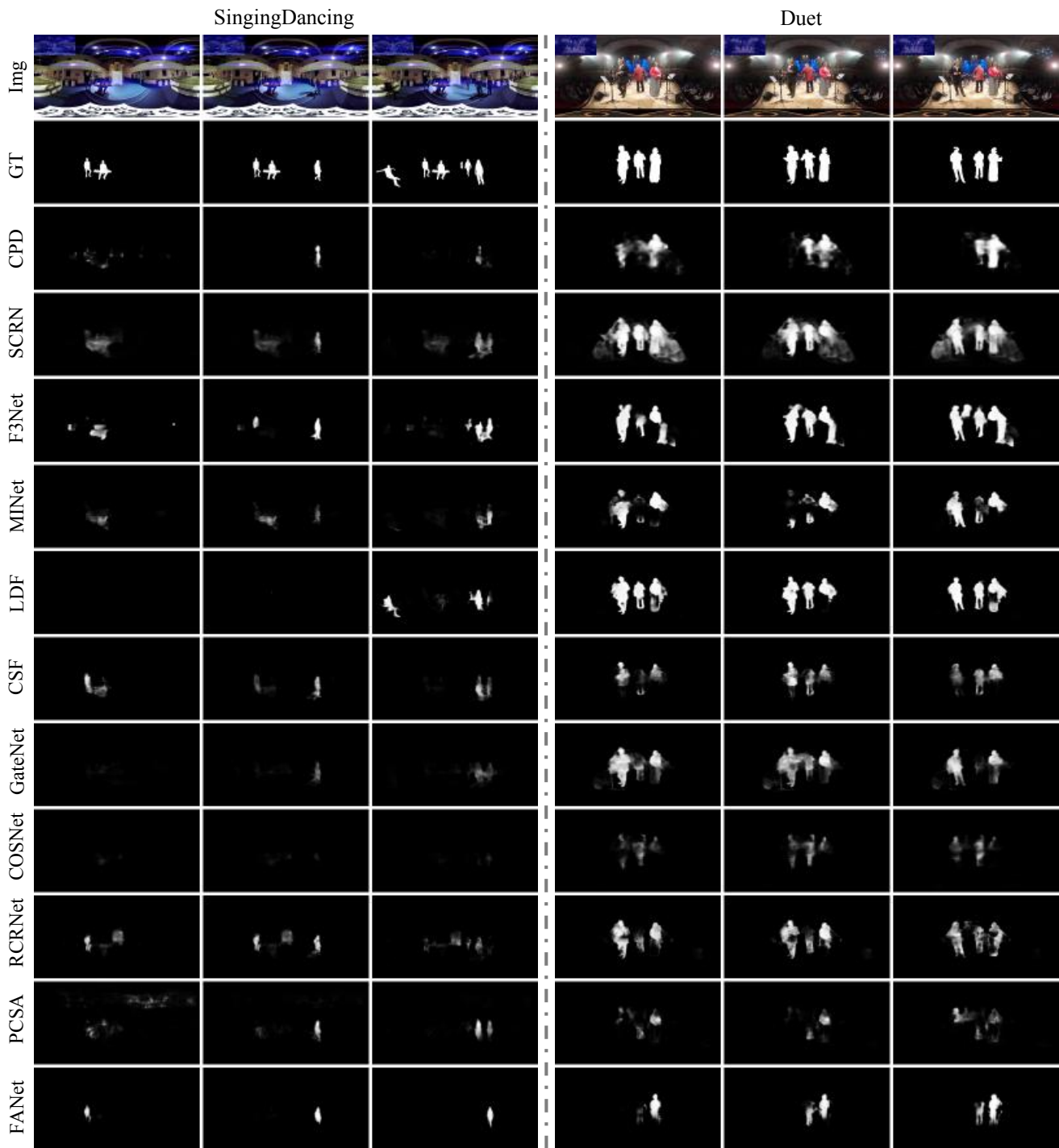


Fig. 15 Visual results of all baselines on the *ASOD60K-test1* (Music). Img = image. GT = ground truth.

- 2018.
- [44] G. Li and Y. Yu. Visual saliency based on multiscale deep features. In *IEEE CVPR*, pages 5455–5463, 2015.
- [45] H. Li, G. Chen, G. Li, and Y. Yizhou. Motion guided attention for video saliency object detection. In *IEEE ICCV*, 2019.
- [46] J. Li, J. Su, C. Xia, and Y. Tian. Distortion-adaptive saliency object detection in 360° omnidirectional images. *IEEE JSTSP*, 14(1):38–48, 2020.
- [47] J. Li, C. Xia, and X. Chen. A benchmark dataset and saliency-guided stacked autoencoders for video-based saliency object detection. *IEEE TIP*, 27(1):349–364, 2018.

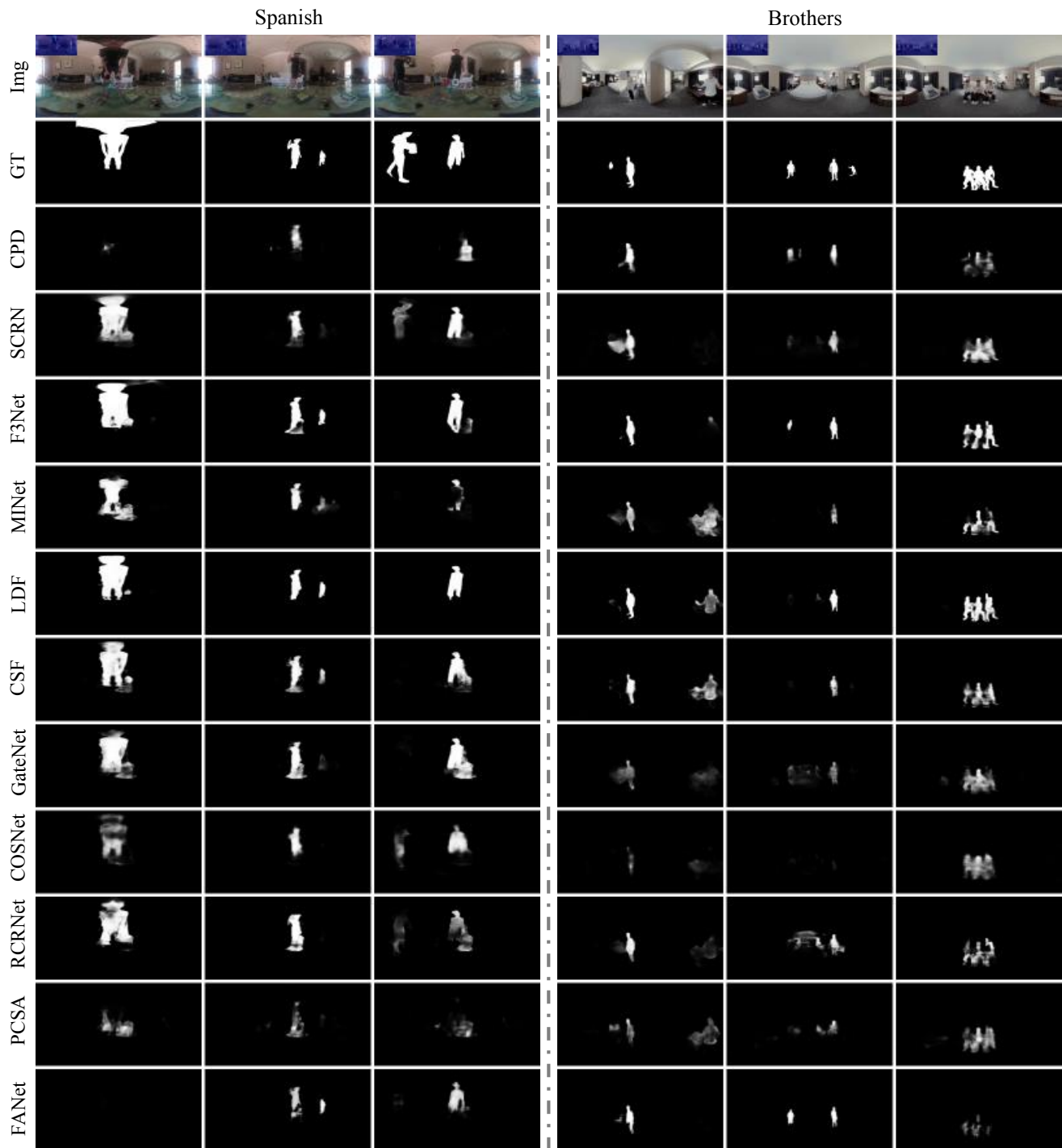


Fig. 16 Visual results of all baselines on the *ASOD60K-test2* (Speaking). Img = image. GT = ground truth.

- [48] Y. Li, X. Hou, C. Koch, J. M. Rehg, and A. L. Yuille. The secrets of salient object segmentation. In *IEEE CVPR*, pages 280–287, 2014.
- [49] J.-J. Liu, Q. Hou, M.-M. Cheng, J. Feng, and J. Jiang. A simple pooling-based design for real-time salient object detection. In *IEEE CVPR*, 2019.
- [50] N. Liu, N. Zhang, L. Shao, and J. Han. Learning selective mutual attention and contrast for rgb-d saliency detection. In *IEEE CVPR*, 2020.
- [51] Z. Liu, J. Li, L. Ye, G. Sun, and L. Shen. Saliency detection for unconstrained videos using superpixel-level graph and spatiotemporal propagation. *IEEE TCSVT*, 27(12):2527–2542, 2017.
- [52] X. Lu, W. Wang, C. Ma, J. Shen, L. Shao, and

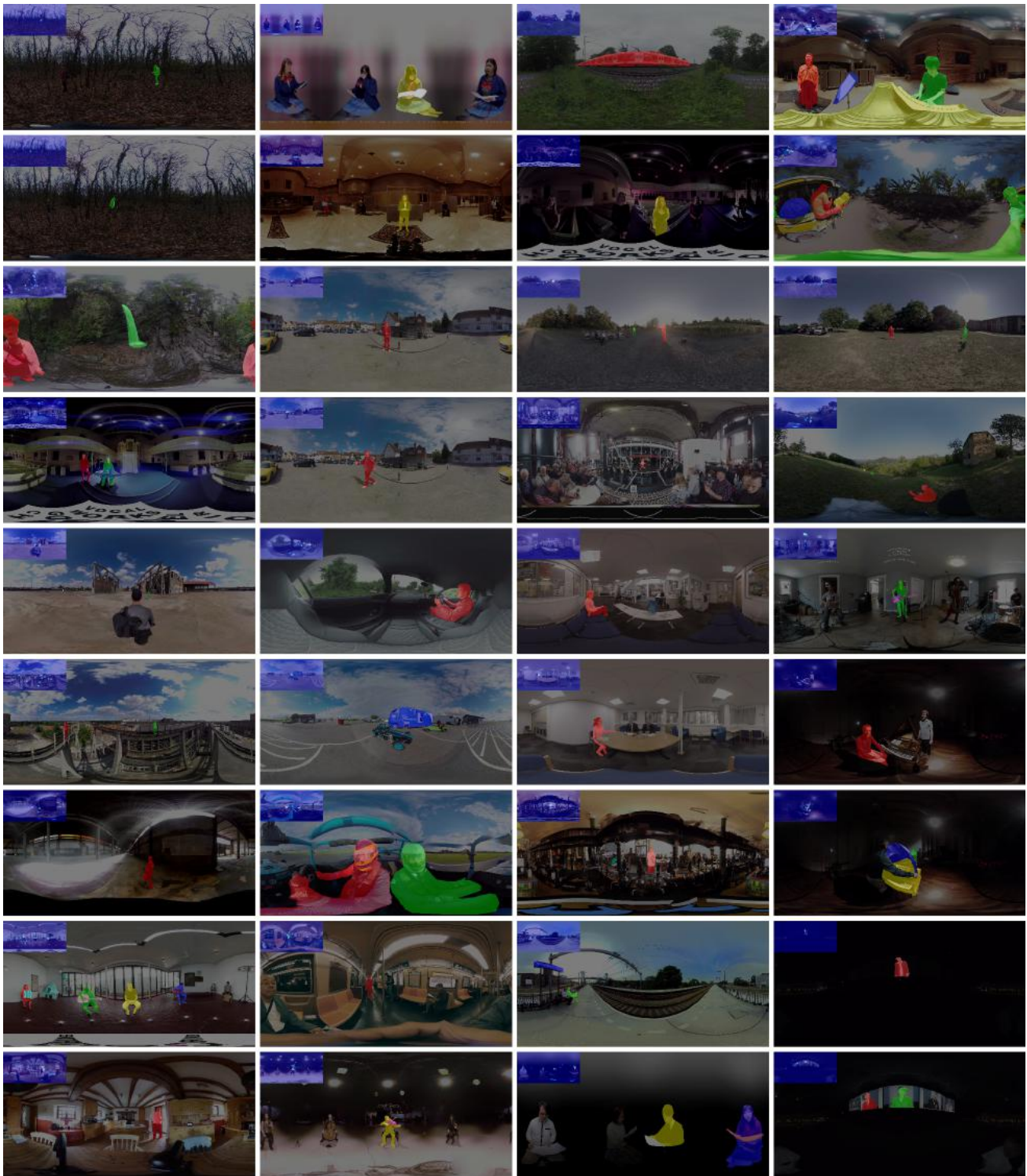


Fig. 17 Sample key frames from *ASOD60K*, with fixations and instance-level ground truth overlaid.

F. Porikli. See more, know more: Unsupervised video object segmentation with co-attention siamese networks. In *IEEE CVPR*, 2019.

[53] G. Ma, S. Li, C. Chen, A. Hao, and H. Qin. Stage-wise salient object detection in 360° omnidirectional image

via object-level semantical saliency ranking. *IEEE TVCG*, 26(12):3535–3545, 2020.

[54] P. Ochs, J. Malik, and T. Brox. Segmentation of moving objects by long term video analysis. *IEEE TPAMI*, 36(6):1187–1200, 2014.

- [55] Y. Pang, X. Zhao, L. Zhang, and H. Lu. Multi-scale interactive network for salient object detection. In *IEEE CVPR*, pages 9413–9422, 2020.
- [56] T. L. Pedro Morgado, Nuno Vasconcelos and O. Wang. Self-supervised generation of spatial audio for 360° video. In *NeurIPS*, 2018.
- [57] F. Perazzi, P. Krähenbühl, Y. Pritch, and A. Hornung. Saliency filters: Contrast based filtering for salient region detection. In *IEEE CVPR*, pages 733–740, 2012.
- [58] F. Perazzi, J. Pont-Tuset, B. McWilliams, L. Van Gool, M. Gross, and A. Sorkine-Hornung. A benchmark dataset and evaluation methodology for video object segmentation. In *IEEE CVPR*, pages 724–732, 2016.
- [59] Y. Piao, W. Ji, J. Li, M. Zhang, and H. Lu. Depth-induced multi-scale recurrent attention network for saliency detection. In *IEEE ICCV*, pages 7254–7263, 2019.
- [60] Y. Piao, Z. Rong, S. Xu, M. Zhang, and H. Lu. Dutsaliency: Versatile dataset and light field-to-rgb saliency detection. *arXiv preprint arXiv:2012.15124*, 2020.
- [61] X. Qin, D.-P. Fan, C. Huang, C. Diagne, Z. Zhang, A. C. Sant’Anna, A. Suárez, M. Jagersand, and L. Shao. Boundary-aware segmentation network for mobile and web applications. *arXiv preprint arXiv:2101.04704*, 2021.
- [62] X. Qin, Z. Zhang, C. Huang, C. Gao, M. Dehghan, and M. Jagersand. Basnet: Boundary-aware salient object detection. In *IEEE CVPR*, 2019.
- [63] Y. Rai, J. Gutiérrez, and P. Le Callet. A dataset of head and eye movements for 360 degree images. In *ACM MMSys*, pages 205–210, 2017.
- [64] K. Simonyan and A. Zisserman. Very deep convolutional networks for large-scale image recognition. In *ICLR*, 2015.
- [65] Y.-C. Su and K. Grauman. Learning spherical convolution for fast features from 360 imagery. In *NeurIPS*, pages 529–539, 2017.
- [66] Y.-C. Su and K. Grauman. Kernel transformer networks for compact spherical convolution. In *IEEE CVPR*, pages 9442–9451, 2019.
- [67] Y.-C. Su, D. Jayaraman, and K. Grauman. Pano2vid: Automatic cinematography for watching 360° videos. In *ACCV*, pages 154–171, 2016.
- [68] J. Tang, D. Fan, X. Wang, Z. Tu, and C. Li. Rgbt salient object detection: benchmark and a novel cooperative ranking approach. *IEEE TCSVT*, 30(12):4421–4433, 2019.
- [69] H. R. Tavakoli, A. Borji, E. Rahtu, and J. Kannala. Dave: A deep audio-visual embedding for dynamic saliency prediction. *arXiv preprint arXiv:1905.10693*, 2019.
- [70] A. Tsiami, P. Koutras, and P. Maragos. Stavis: Spatio-temporal audiovisual saliency network. In *IEEE CVPR*, pages 4766–4776, 2020.
- [71] Z. Tu, T. Xia, C. Li, X. Wang, Y. Ma, and J. Tang. Rgb-t image saliency detection via collaborative graph learning. *IEEE TMM*, 22(1):160–173, 2019.
- [72] E. Van der Burg, C. N. Olivers, A. W. Bronkhorst, and J. Theeuwes. Audiovisual events capture attention: Evidence from temporal order judgments. *JOV*, 8(5):2–2, 2008.
- [73] A. B. Vasudevan, D. Dai, and L. Van Gool. Semantic object prediction and spatial sound super-resolution with binaural sounds. In *ECCV*, pages 638–655, 2020.
- [74] G. Wang, C. Chen, D.-P. Fan, A. Hao, and H. Qin. From semantic categories to fixations: A novel weakly-supervised visual-auditory saliency detection approach. In *IEEE CVPR*, pages 15119–15128, 2021.
- [75] L. Wang, H. Lu, Y. Wang, M. Feng, D. Wang, B. Yin, and X. Ruan. Learning to detect salient objects with image-level supervision. In *IEEE CVPR*, pages 136–145, 2017.
- [76] W. Wang, Q. Lai, H. Fu, J. Shen, H. Ling, and R. Yang. Salient object detection in the deep learning era: An in-depth survey. *IEEE TPAMI*, 2021.
- [77] W. Wang, J. Shen, X. Dong, and A. Borji. Salient object detection driven by fixation prediction. In *IEEE CVPR*, pages 1711–1720, 2018.
- [78] W. Wang, J. Shen, F. Guo, M.-M. Cheng, and A. Borji. Revisiting video saliency: A large-scale benchmark and a new model. In *IEEE CVPR*, pages 4894–4903, 2018.
- [79] W. Wang, J. Shen, and L. Shao. Consistent video saliency using local gradient flow optimization and global refinement. *IEEE TIP*, 24(11):4185–4196, 2015.
- [80] J. Wei, S. Wang, Z. Wu, C. Su, Q. Huang, and Q. Tian. Label decoupling framework for salient object detection. In *IEEE CVPR*, pages 13025–13034, 2020.
- [81] C. Wu, R. Zhang, Z. Wang, and L. Sun. A spherical convolution approach for learning long term viewport prediction in 360 immersive video. In *AAAI*, pages 14003–14040, 2020.
- [82] Z. Wu, L. Su, and Q. Huang. Cascaded partial decoder for fast and accurate salient object detection. In *IEEE CVPR*, pages 3907–3916, 2019.
- [83] Z. Wu, L. Su, and Q. Huang. Stacked cross refinement network for edge-aware salient object detection. In *IEEE ICCV*, pages 7264–7273, 2019.
- [84] M. Xu, C. Li, S. Zhang, and P. Le Callet. State-of-the-art in 360 video/image processing: Perception, assessment and compression. *IEEE JSTSP*, 14(1):5–26, 2020.
- [85] M. Xu, Y. Song, J. Wang, M. Qiao, L. Huo, and Z. Wang. Predicting head movement in panoramic video: A deep reinforcement learning approach. *IEEE TPAMI*, 41(11):2693–2708, 2019.
- [86] Y. Xu, Y. Dong, J. Wu, Z. Sun, Z. Shi, J. Yu, and S. Gao. Gaze prediction in dynamic 360 immersive videos. In *IEEE CVPR*, pages 5333–5342, 2018.
- [87] P. Yan, G. Li, Y. Xie, Z. Li, C. Wang, T. Chen, and L. Lin. Semi-supervised video salient object detection

- using pseudo-labels. In *IEEE ICCV*, pages 7284–7293, 2019.
- [88] Q. Yan, L. Xu, J. Shi, and J. Jia. Hierarchical saliency detection. In *IEEE CVPR*, pages 1155–1162, 2013.
- [89] C. Yang, L. Zhang, H. Lu, X. Ruan, and M.-H. Yang. Saliency detection via graph-based manifold ranking. In *IEEE CVPR*, pages 3166–3173, 2013.
- [90] W. Yang, Y. Qian, J.-K. Kamarainen, F. Cricri, and L. Fan. Object detection in equirectangular panorama. In *IEEE ICPR*, pages 2190–2195, 2018.
- [91] Y. Zeng, P. Zhang, J. Zhang, Z. Lin, and H. Lu. Towards high-resolution salient object detection. In *IEEE ICCV*, pages 7234–7243, 2019.
- [92] C. Zhang, S. Liwicki, W. Smith, and R. Cipolla. Orientation-aware semantic segmentation on icosahedron spheres. In *IEEE ICCV*, pages 3533–3541, 2019.
- [93] P. Zhang, W. Liu, Y. Zeng, Y. Lei, and H. Lu. Looking for the detail and context devils: High-resolution salient object detection. *IEEE TIP*, 2021.
- [94] Q. Zhang, R. Cong, C. Li, M.-M. Cheng, Y. Fang, X. Cao, Y. Zhao, and S. Kwong. Dense attention fluid network for salient object detection in optical remote sensing images. *IEEE TIP*, 2020.
- [95] Y. Zhang, L. Zhang, W. Hamidouche, and O. Deforges. A fixation-based 360° benchmark dataset for salient object detection. In *IEEE ICIP*, 2020.
- [96] Z. Zhang, Y. Xu, J. Yu, and S. Gao. Saliency detection in 360 videos. In *ECCV*, pages 488–503, 2018.
- [97] J.-X. Zhao, J.-J. Liu, D.-P. Fan, Y. Cao, J. Yang, and M.-M. Cheng. Egnnet: Edge guidance network for salient object detection. In *IEEE ICCV*, pages 8779–8788, 2019.
- [98] P. Zhao, A. You, Y. Zhang, J. Liu, K. Bian, and Y. Tong. Spherical criteria for fast and accurate 360° object detection. In *AAAI*, pages 12959–12966, 2020.
- [99] X. Zhao, Y. Pang, L. Zhang, H. Lu, and L. Zhang. Suppress and balance: A simple gated network for salient object detection. In *ECCV*, 2020.
- [100] H. Zhou, X. Xie, J.-H. Lai, Z. Chen, and L. Yang. Interactive two-stream decoder for accurate and fast saliency detection. In *IEEE CVPR*, pages 9141–9150, 2020.
- [101] T. Zhou, D.-P. Fan, M.-M. Cheng, J. Shen, and L. Shao. Rgb-d salient object detection: A survey. *CVMMJ*, pages 1–33, 2021.
- [102] M. Zhuge, D.-P. Fan, N. Liu, D. Zhang, D. Xu, and L. Shao. Salient object detection via integrity learning. *arXiv preprint arXiv:2101.07663*, 2021.
- [103] C. Zuyao, X. Qianqian, C. Runmin, and H. Qingming. Global context-aware progressive aggregation network for salient object detection. In *AAAI*, 2020.



Yi Zhang received his bachelor degree in 2016 and master degree in 2019 respectively from Southeast University both in biomedical engineering. He is pursuing his PhD degree at INSA

Rennes, France. His current research interests include omnidirectional vision, salient object detection, camouflaged object detection and deep learning.